PHYSICAL REVIEW A **66**, 063816 (2002)

Theory of optical near-resonant cone emission in atomic vapor

B. D. Paul, J. Cooper, and A. Gallagher
JILA, National Institute of Standards and Technology, Boulder, Colorado 80309-0440
and University of Colorado, Boulder, Colorado 80309-0440

M. G. Raymer
Oregon Center for Optics and Department of Physics, University of Oregon, Eugene, Oregon 97403

(Received 16 March 2001; revised manuscript received 9 July 2002; published 31 December 2002)

A time-dependent theory for conical emission during near-resonant propagation of laser light in an atomic vapor, which includes full propagation for the laser and frequency sidebands in a nonlinear two-level medium is presented. The density-matrix equations for the dipole moment and population are solved in the dressed atomic frame. The polarization source terms are accurate to order $\gamma/\mathcal{R}$, where γ is a damping constant and $\mathcal{R}$ is the generalized Rabi frequency. Analytical plane-wave solutions and numerical, cylindrically symmetric propagation simulations including diffraction are presented. It is shown that the calculations with cylindrically symmetric fields and atomic excitation profiles are incapable of accounting for the high levels of optical gain that are responsible for the intense conical emission observed in experiments. This result is at first surprising, since the model accounts rigorously for all of the physical phenomena that have been previously proposed as being responsible for generating large gains, and the calculation matches the symmetry of the observations. The lack of large calculated gain seems to imply the existence of higher-order $(m>0)$ radial modes in the field for the experimental conditions that give rise to cone emission. In the simulations, however, the cylindrically symmetric fields do produce weak red-detuned cones with angular-frequency distributions similar to those seen in experiments.

DOI: 10.1103/PhysRevA.66.063816 PACS number(s): 42.65.Sf, 42.65.Tg, 42.65.Hw

I. INTRODUCTION

When a blue-detuned, intense, near-resonant laser beam propagates through an atomic vapor, a diffuse ring of light may be observed around the laser spot in the far field. This phenomenon has been referred to as conical emission or cone emission (CE). Spectral analysis shows that the CE is separated from the atomic resonance by approximately the laser detuning, but is on the opposite (red) side of the resonance.

The cause of CE from a pulsed-laser excited atomic vapor is the subject of this paper. However, the observation of a ring of light around a far-field laser beam is not unique to atomic vapors and has different causes in different cases. For example, CE from glasses has been observed in the presence of picosecond (ps) and femtosecond (fs) laser-beam self-focusing; it appears to be reasonably consistent with four-wave mixing (FWM) [1]. The red-detuned and blue-detuned sidebands are presumed to result from Stokes and anti-Stokes Raman transitions, and both sidebands emerge at cone angles related to FWM phase matching. The medium is presumed to be weakly saturated, sufficient to confine the self-focused beam but not to significantly modify the index of refraction variation versus wavelength. Another example of CE results from spatial self-phase modulation [2]. Here different radial intensities pick up different amounts of phase during propagation through the nonlinear medium, resulting in rings (CE) in the far field around the central laser spot. These rings are at the same frequency as the laser.

CE in atomic vapors has generally been observed using pulsed lasers of 2–15-ns pulse length. Such studies have been conducted in sodium vapor [3–12], potassium [13], barium [2,14–16], cesium [2], calcium [17], and strontium [18,19]. This CE is normally, but not always [5,6,19,20], observed with blue laser detuning, a detuning that can also yield self-focusing. In most of these experiments self-focusing or its absence was not measured, but where it was measured it was found to be necessary for the formation of CE [8,21,22]. One experiment has demonstrated that atomic vapor CE can be produced by ps laser pulses, but not by fs pulses [23].

One CE experiment using a cw laser has been reported by Valley *et al.* [24]. The laser was blue detuned by an amount comparable to the Doppler width, and the beam was self-focused in sodium vapor. Rabi sidebands on the red and blue side of the laser frequency were observed in the forward direction, with the red sideband in a cone. This paper includes a brief description of a very detailed calculation of FWM within this self-focused region of the vapor. Although the laser beam is cylindrically symmetric, the calculation does not impose cylindrical symmetry. Random noise in the form of resonance fluorescence is added for each frequency and location by using plasma-dispersion functions. They show that this noise stimulates coherent gain for both sidebands via four-wave mixing. The red-detuned sideband forms a cone and the blue-detuned sideband propagates along the axis, receiving greater gain. The results of the calculation agreed with the character of their observed forward emission. Thus, it appears that CE induced by cw pumping very close to resonance results from FWM gain, combined with propagation effects in the strongly driven region of a self-focused laser beam.

Four-wave mixing of Rabi sidebands has also been invoked to explain pulsed-laser CE from atomic vapors pumped far from resonance. But there is a problem with this explanation for the atomic vapor experiments with ns pulsed lasers; in the experiments the blue-detuned Rabi sideband required for FWM is usually missing from the forward emission [19]. In these pulsed-laser experiments, the laser is detuned many Doppler widths to the blue side of the atomic transition and has negligible Fourier components at the resonance frequency. The CE, on the red side of the atomic line, emerges at an average angle that can be represented by either a phase-matching condition or refraction at the boundary between a saturated and an unsaturated medium. This has led to suggestions of a Cherenkov-type process (phase matching) [9,25,26] or Rabi sideband generation in the saturated region and boundary refraction [27]. However, these suggestions, as well as all FWM calculations, have not solved the problems of the experimentally missing blue sideband or of how to obtain the large observed CE intensities within a self-focused filament. They are also inconsistent with several features of the full frequency versus angular spectrum [19].

The most viable basis for explaining pulsed-laser CE appears in a paper by Crenshaw and Cantrell [28]. They demonstrated theoretically that a short ($\tau_{\mathrm{FWHM}}=125$ ps) self-focused, blue-detuned pulse undergoes spatial temporal breakup and develops a small angularly and (somewhat) spectrally isolated component at negative detuning from the laser frequency. They suggest that this component is CE, but computational limitations prevented propagating the pulse sufficient distance to actually place it on the red side of resonance or to see if its frequency saturates at an appropriate value for CE. In addition, the intensity of this predicted "CE" component is far below the several percents of the laser pulse that is observed, and they assert that it will not grow with further propagation. This implies that some additional mechanisms are necessary to yield the experimentally observed strong CE. Their short pulse (used for computational ease) also has a much broader Fourier spectrum than the experimental ns pulses, which are well isolated from resonance. Thus, while this calculation demonstrates interesting pulse breakup and generation of new forward-propagating frequencies, it leaves major unresolved questions. Guo *et al.* [29] addressed some of these in a plane-wave transient-pulse-breakup calculation. This calculation yielded spectral components of more reasonable intensity and at easily understood frequencies: the Rabi sidebands. However, without inclusion of the intensity variations within a self-focused filament these sideband intensities and frequencies may be misleading, and in addition, in this calculation both sidebands were generated with comparable intensities, that are at odds with experiments.

Thus, although scores of calculations have been published regarding CE in atomic vapors, even very basic questions regarding the causes and behavior of pulsed CE generation have not been answered. The primary issue investigated here is how sufficient sideband gain can occur within a self-focused filament to yield the measured CE intensities. These sidebands are distinctly separated from the laser frequency and propagate in a medium modified by the much stronger, self-focused laser beam. We develop equations describing the full spatial and temporal evolution of a self-focused laser beam and copropagating sidebands. However, because of computational constraints we only solve these here for steady-state beams. This cw solution involves similar conditions and equations to those investigated by Valley *et al.* [47]. However, there are a few key differences. As a result of the greater intensities involved in pulsed-laser experiments, the area of optimal interaction between systemically detuned sidebands is smaller than cw experiments. Even though both works use a cylindrical symmetric input field, ours is restricted to cylindrical symmetry, whereas the Valley *et al.* calculations were done on an *x-y* grid allowing nonsymmetrical fields.

The calculations presented here are for the case of a single self-focused filament, whereas CE is often seen with beam breakup into multiple, copropagating, self-focused filaments. However, in Ref. [22] great care was taken to observe cones from single filaments, and the present calculations will be compared to that experiment. The theory presented here is valid for beam breakup, but only calculations for single self-focused filaments will be presented.

The model we develop below accounts for longitudinal and transverse propagation of laser and sidebands in the presence diffraction and the laser modified medium, including Doppler broadening. The density-matrix equations for the atomic response are solved self-consistently with the field wave equations. To facilitate computational speed, the time-dependent propagation equations are solved in steady state with a constraint of cylindrical symmetry. The model accounts rigorously for all of the physical phenomena that have been previously proposed for generating the large observed gains. Four-wave mixing and Cherenkov-type processes are automatically included, without requiring any *a priori* appeal to specific mechanisms. We also present an extension to a plane-wave model presented by Boyd *et al.* [30].

The equations of motion are derived in Sec. II. Selected solutions to the equations of motion are presented in Sec. III. Simple plane-wave solutions, which give insight to the more complicated numerical solutions, are presented in Sec. III A. Section III B gives examples of cylindrically symmetric solutions with diffraction. The discussion in Sec. IV presents cone spectra and comments on the paucity of observed gain. Noncylindrically symmetric solutions and their implications for sideband gain are also discussed here.

II. EQUATIONS OF MOTION

The electric field of the laser is assumed to be linearly polarized in the $\hat{x}$ direction and to be propagating in the $\hat{z}$ direction. (Experimentally it is known that the field remains polarized.) This allows the electric field **E** and the polarization **P** to be written in the following form:

$$\mathbf{E}=E\hat{x}=\frac{1}{2}[\varepsilon(x,y,z,t)e^{i(\omega_l t-\mathbf{K}_l\cdot\mathbf{z})}+\text{c.c.}]\hat{x}, \tag{1a}$$

$$\mathbf{P}=P\hat{x}=\frac{1}{2}[\mathcal{P}(x,y,z,t)e^{i(\omega_l t-\mathbf{K}_l\cdot\mathbf{z})}+\text{c.c.}]\hat{x}, \tag{1b}$$

where ε and $\mathcal{P}$ are the envelope functions for the field and the polarization, respectively, ω_l is the frequency of the laser, and $\mathbf{K}_l$ is the free-space wave number. The slowly varying envelope approximation (SVEA) [31] is used to derive an equation of motion for ε. All variations of the wave number from the free-space wave number are contained inside the envelope function ε. This does not violate the SVEA because the magnitude of the index of refraction involved in this problem is near unity ($|n-1|\sim 10^{-5}$).

The atomic medium is treated as a closed two-level system with an excited state $|e\rangle$ and a ground state $|g\rangle$ which have an energy separation of $\hbar\omega_0$. Equations of motion for the population inversion $d=\rho_{ee}-\rho_{gg}$ and ρ_{eg}, where ρ_{ij} are elements of the density matrix, can be written as follows:

$$\dot{d}=-2i\frac{\wp E}{\hbar}(\rho_{eg}-\rho_{eg}^{*})-\Gamma(d-d_o), \tag{2a}$$

$$\dot{\rho}_{eg}=-(\gamma+i\omega_0)\rho_{eg}-i\frac{\wp E}{\hbar}d, \tag{2b}$$

where $\wp$ is the dipole matrix element between $|e\rangle$ and $|g\rangle$. The decay rates Γ and $\gamma=\Gamma/2+\gamma_c$ correspond to the population radiative decay rate and the dipole dephasing rate, respectively. The dephasing rate due to collisions is γ_c. The atomic variables will be labeled by atomic velocity v. Using the concept of a convective derivative and the rotating wave approximation (RWA) with the substitutions

$$\rho_{eg}=\rho e^{-i(\omega_l t-K_l z)}e^{-i\Phi} \quad \text{and} \quad \frac{\varepsilon\wp}{\hbar}=|\Omega|e^{i\Phi}, \tag{3}$$

Eq. (2) can be rewritten as

$$\frac{\partial d(v)}{\partial t}=-i|\Omega|[\rho(v)-\rho^{*}(v)]-\Gamma(d(v)+1), \tag{4a}$$

$$\frac{\partial \rho(v)}{\partial t}=-(\gamma-i\Delta)\rho(v)-\frac{i}{2}|\Omega|d(v), \tag{4b}$$

where $\Delta=\Delta_0+\dot{\Phi}-K_l v$ and $\Delta_0=\omega_l-\omega_0$. The phase of the laser Φ is explicitly included in Eq. (3) to facilitate the inclusion of phase fluctuations. The polarization $\mathcal{P}$ may be expressed in terms of $\rho(v)$ as

$$\mathcal{P}=2\wp N\int_{-\infty}^{\infty}\rho^{*}(v)W(v)e^{-i\Phi}dv, \tag{5}$$

where N is the number density and $W(v)$ is the normalized velocity distribution in the $\hat{z}$ direction. It should be kept in mind that $\mathcal{P}$ and $\rho(v)$ are both functions of x, y, z, and t. The SVEA Maxwell wave equation for the Rabi frequency (Ω) is

$$\frac{\partial\Omega}{\partial z}=-\frac{i\lambda}{4\pi}\nabla_{\perp}^{2}\Omega-\frac{3i}{4\pi}N\lambda^{2}\Gamma\int_{-\infty}^{\infty}\rho^{*}(v)W(v)e^{-i\Phi}dv, \tag{6}$$

where $\nabla_{\perp}^{2}$ is the transverse Laplacian, and the relationship

$$|\wp|^{2}=\frac{3\pi\varepsilon_o\hbar c^{3}\Gamma}{\omega_o^{3}} \tag{7}$$

corresponding to a $J_g=0$ to $J_e=1$ transition was used.

The longitudinal and radial coordinates $(z,\tilde{r})$ can be transformed into dimensionless parameters (ζ,r) via the following transformations:

$$\zeta=\eta z=\left[\frac{3N\lambda^{2}\Gamma}{8\pi|\Delta_0|}\right]z, \tag{8a}$$

$$r=\sigma_r\tilde{r}=\left[\sqrt{\frac{3N\lambda\Gamma}{2|\Delta_0|}}\right]\tilde{r}. \tag{8b}$$

These transformations allow Eq. (6) to be rewritten in the following form:

$$\frac{\partial\Omega}{\partial\zeta}=-i\nabla_{\perp}^{2}\Omega-2i|\Delta_o|\int_{-\infty}^{\infty}\rho^{*}(v)W(v)e^{i\Phi}dv. \tag{9}$$

A motivation and explanation of the dimensionless parameter space is given in Refs. [22] and [32].

A. Input field

In the model presented, sideband fields are imposed at the cell entrance, not generated within the cell. The details of a more realistic sideband seed for initiation are quite involved and are not dealt with here, although a brief overview will be presented. (For the details of the quantum mechanics of the seed, see You [33].)

Amplified spontaneous emission (ASE), spontaneous emission (SE), and Fourier components of the laser-pulse envelope are the three main candidates for the sideband seed. The first two, ASE and SE, are purely quantum mechanical in nature. ASE is broadband stochastic light that originates in the laser and is incident on the input face of the cell, as opposed to SE, which may start at any location in the cell. It has been shown that both of these processes can be modeled as a stochastic input field at the beginning of the cell [34]. The third seeding possibility, the Fourier components of the input laser pulse, is obviously a field that can be applied as a seed at the input plane of the cell. This allows the full input field, expressed as a Rabi frequency, to be written as

$$\Omega(r,t)=[|\Omega_l(r,t)|+\Omega_r(r,t)+\Omega_b(r,t)]e^{i\Phi}, \tag{10}$$

where the fields $\Omega_r(r,t)$ and $\Omega_b(r,t)$ are stochastic fields generated by methods described by You [33]. The input field may be expanded in Fourier components as

$$\Omega(r,t)=\left[|\Omega_l(r,t)|+\sum_n a_n e^{-i(\mathcal{R}_0+\delta_n)t}+\sum_m b_m e^{i(\mathcal{R}_0+\delta_m)t}\right]e^{i\Phi}, \tag{11}$$

where the a_n and b_m depend on the statistics of the seed and δ_n and δ_m are the detunings of the red and blue sidebands relative to $\mp\mathcal{R}$, respectively. For both ASE and SE,

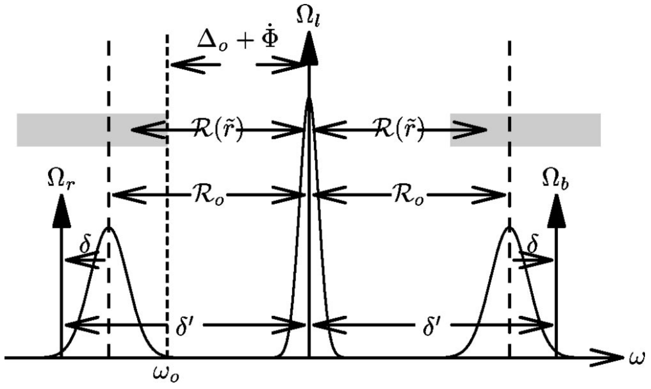

FIG. 1. Definition of terms in frequency space. The short-dashed line at ω_0 is the atomic line. The incident laser beam has an on-axis intensity of $|\Omega_l|^2$ and is detuned to the blue side of the atomic line by $\Delta_0+\dot{\Phi}$. On either side of the laser are the weak sidebands, Ω_r and Ω_b. The generalized Rabi frequency $\mathcal{R}_0$ is measured with the maximum Ω_l at the center of the beam at the input of the vapor. The generalized Rabi frequency $\mathcal{R}(\tilde{r})$ is a function of time and space and is usually within the gray region. The sidebands are shown here as symmetrically detuned about the laser by δ', and $\delta=\delta'-\mathcal{R}_0$.

$\langle a_n^* \, a_{n'}\rangle=\delta_{nn'}$ and $\langle b_n^* \, b_{n'}\rangle=\delta_{nn'}$, where $\langle\,\rangle$ indicates a stochastic average. For ASE, $\langle a_n^* \, b_{n'}\rangle=0$ whereas for SE, $\langle a_n^* \, b_{n'}\rangle\neq 0$. The sidebands are assumed to be clustered around the frequencies $\pm\mathcal{R}_o$. The relationship between different frequencies are shown in Fig. 1. It is unnecessary to specify values for the initial intensities of the sidebands because the model presented here is linear in the sideband fields.

The three fields of Eq. (10) may be put into Eqs. (4a) and (4b), giving

$$\frac{\partial d}{\partial t}=-i\{[|\Omega_l|+\Omega_r(r,t)+\Omega_b(r,t)]\rho-[|\Omega_l|+\Omega_r^*(r,t)+\Omega_b^*(r,t)]\rho^*\}-\Gamma(d+1), \tag{12a}$$

$$\frac{\partial \rho}{\partial t}=-(\gamma-i\Delta)\rho-i\frac{d}{2}[|\Omega_l|+\Omega_r^*(r,t)+\Omega_b^*(r,t)]. \tag{12b}$$

These equations are coupled via $|\Omega_l|$, which can be arbitrarily large. To remove this strong coupling, these equations are transformed into a dressed frame. The dressed states are defined as

$$|1\rangle=b_2|e\rangle+b_1|g\rangle, \tag{13a}$$

$$|2\rangle=b_1|e\rangle-b_2|g\rangle, \tag{13b}$$

where the coefficients b_1 and b_2 are defined in terms of the generalized Rabi frequency ($\mathcal{R}=\sqrt{|\Omega|^2+\Delta^2}$) as

$$b_1=\sqrt{\frac{\mathcal{R}+\Delta}{2\mathcal{R}}}, \tag{14a}$$

$$b_2=-\sqrt{\frac{\mathcal{R}-\Delta}{2\mathcal{R}}}. \tag{14b}$$

Using these transformations it is possible to write equations that transform the bare population inversion (d) and the off-diagonal density-matrix element (ρ) into the dressed population inversion ($\mathcal{D}$) and the dressed off-diagonal density-matrix element (σ),

$$\mathcal{D}=d(b_1^2-b_2^2)-2(\rho+\rho^*)b_1b_2, \tag{15a}$$

$$\sigma=\rho^*b_1^2-\rho b_2^2+db_1b_2. \tag{15b}$$

Equations of motion for $\mathcal{D}$ and σ can be derived by placing Eqs. (12a) and (12b) into Eqs. (15a) and (15b), then performing a time derivative resulting in the following equations:

$$\frac{\partial \mathcal{D}}{\partial t}=-\tilde{g}\mathcal{D}-f+2q_+(\sigma+\sigma^*)-\frac{i}{4}\frac{|\Omega_l|^2}{\mathcal{R}^2}(\Omega_s-\Omega_s^*)(\sigma+\sigma^*)+i[(\Omega_s^*b_2^4-\Omega_sb_1^4)\sigma^*+(\Omega_s^*b_1^4-\Omega_sb_2^4)\sigma], \tag{16a}$$

$$\frac{\partial \sigma}{\partial t}=-(a+i\mathcal{R})\sigma+\chi+q_-\mathcal{D}+v\sigma^*+\frac{i}{2}(\Omega_sb_1^2-\Omega_s^*b_2^2)\mathcal{D}-\frac{i}{2}\frac{|\Omega_l|}{\mathcal{R}}(\Omega_s+\Omega_s^*)\sigma, \tag{16b}$$

where $\Omega_s=\Omega_r(r,t)+\Omega_b(r,t)$ and

$$\tilde{g}=\frac{1}{\mathcal{R}^2}(\gamma|\Omega_l|^2+\Gamma\Delta^2), \tag{17a}$$

$$f=\frac{\Gamma\Delta}{\mathcal{R}}, \tag{17b}$$

$$q_\pm=\frac{1}{2\mathcal{R}^2}\left(\pm\Delta\frac{d}{dt}|\Omega_l|+|\Omega_l|\ddot{\Phi}-|\Omega_l|\Delta(\gamma-\Gamma)\right), \tag{17c}$$

$$a=\frac{1}{2\mathcal{R}^2}(\gamma\mathcal{R}^2+\gamma\Delta^2+\Gamma|\Omega_l|^2), \tag{17d}$$

$$\chi=\frac{\Gamma|\Omega_l|}{2\mathcal{R}}, \tag{17e}$$

$$\mathrm{v}=\frac{|\Omega_l|^2}{2\mathcal{R}^2}(\gamma-\Gamma). \tag{17f}$$

Notice that all of the quantities defined in Eqs. (17a) through (17f) are of order γ and are functions of space and time. The quantities $\mathcal{R}$ and Δ are of the same order of magnitude and are assumed to be large in comparison to the decay rates (γ and Γ). The quantity Ω_l may take on any value.

Equations (16a) and (16b) can be solved using a perturbation method by letting $\mathcal{D}=\mathcal{D}^{(0)}+\mathcal{D}^{(1)}$ and $\sigma=\sigma^{(0)}+\sigma^{(1)}$ and by using $\gamma/\mathcal{R}$ as the small parameter. The zeroth-order terms contain only the laser propagation because the sidebands are considered as first order, small quantities that do not alter the laser propagation. The equations of motion for $\mathcal{D}^{(0)}$ and $\sigma^{(0)}$, are as follows:

$$\dot{\mathcal{D}}^{(0)} = -\tilde{g}\mathcal{D}^{(0)} - f, \tag{18a}$$

$$\sigma^{(0)} \approx \frac{\chi + q_- \mathcal{D}^{(0)}}{(a + i\mathcal{R})}, \tag{18b}$$

where weak coupling via the terms $2q_+[\sigma^{(0)} + (\sigma^{(0)})^*]$ and $v(\sigma^{(0)})^*$ have been dropped. Adiabatic expansion in the dressed frame requires $\tau_r \Delta_0 \gg 1$, where τ_r is the rise time of the laser pulse. This was used in the derivation of Eq. (18b). These equations of motion are good to order $\gamma/\mathcal{R}$. This is a point of departure from the work of Valley *et al.* [47], who produced calculations for relatively small laser detuning that do not allow the assumption that $\gamma/\mathcal{R}$ is a small quantity.

Using Eqs. (18a) and (18b) it is possible to write the following time-dependent equation of motion for the laser-beam Rabi frequency

$$\frac{\partial \Omega_l}{\partial \zeta} = -i\nabla_\perp^2 \Omega_l - \alpha_l(t)\Omega_l, \tag{19}$$

where

$$\alpha_l(t) = \frac{|\Delta_0|}{\mathcal{R}}\left\{ i\mathcal{D}^{(0)} + \frac{1}{\mathcal{R}}\left[\Gamma - \frac{\Delta}{\mathcal{R}}(\gamma - \Gamma)\mathcal{D}^{(0)}\right]\right\}. \tag{20}$$

The self-focusing and time-dependent properties of Eq. (19) are quite involved.

The sidebands are considered as first order, small quantities that do not alter the laser propagation. The only significant contribution to the sideband polarization comes from the $\sigma^{(1)}$ term. The equation of motion for $\sigma^{(1)}$ is as follows:

$$\frac{\partial \sigma^{(1)}}{\partial t} = -(a + i\mathcal{R})\sigma^{(1)} + A[\Omega_r(r,t) + \Omega_b(r,t)] + B[\Omega_r^*(r,t) + \Omega_b^*(r,t)], \tag{21}$$

where

$$A = \frac{i}{2}\left(\mathcal{D}^{(0)} b_1^2 - \frac{|\Omega_l|}{\mathcal{R}}\sigma^{(0)}\right), \tag{22a}$$

$$B = -\frac{i}{2}\left(\mathcal{D}^{(0)} b_2^2 + \frac{|\Omega_l|}{\mathcal{R}}\sigma^{(0)}\right). \tag{22b}$$

As a result of the time dependence of Eq. (21), it is not valid to assume that only symmetrically detuned sidebands couple, as is done in steady-state four-wave mixing. Nonetheless, one would expect that if the coefficients A and B in Eq. (21) are slowly varying, the strongest coupling between the sidebands will still occur for symmetrically detuned sidebands. To investigate coupling between symmetrically detuned sidebands, Eq. (21) may be solved formally, by Fourier transforms, for the special case of Ω_b^* driving Ω_r with the following result:

$$\bar{\sigma}^{(1)}(\delta_r') = -\frac{1}{\sqrt{2\pi}}\int_{-\infty}^{\infty} W(\nu)\int_{-\infty}^{\infty} \frac{B(\omega)\Omega_b^*(r,\omega - \delta_r')}{a + i\left(\mathcal{R} + \nu\frac{\Delta}{\mathcal{R}} - \delta_r'\right)} \times d\omega\, d\nu. \tag{23}$$

The bar over $\sigma^{(1)}$ and any forthcoming variable will denote Doppler averaging. The velocity distribution has been written in terms of frequency as $W(\nu)$. The quantity $B(\omega)$ is the Fourier transform of B in Eq. (22b). The variables δ_r' and δ_b' correspond to the left and right δ''s, respectively, in Fig. 1. This figure assumes that $\delta_r' = \delta_b'$. A similar integral yields $\bar{\sigma}^{(1)}(\delta_b')$ in terms of A and $\Omega_r^*(r,\omega - \delta_b')$. The frequency width of $B(\omega)$ is of the order of the laser-pulse-transformed width (~0.3 GHz). This width can be justified by noticing that each factor in Eq. (22b) is smoothly driven by the laser. The same argument holds for $A(\omega)$. The width of $\Omega_b^*(r,\omega - \delta_r')$ is of the order of the Doppler averaged gain width (~8 GHz). This width is inferred from the plane-wave solutions presented in Sec. III A. With $B(\omega)$ much narrower than $\Omega_b^*(r,\omega - \delta_r')$ it is possible to pull $\Omega_b^*(r,\omega - \delta_r')$ outside of the integral and evaluate it at $\omega = 0$. Under this set of approximations only symmetrically detuned sidebands couple. Also, from a numerical standpoint the problem becomes much more tractable. A complete derivation of Eq. (23) may be found in Ref. [35].

B. Sideband equations of motion

As a result of only considering symmetrically detuned sidebands only one sum in Eq. (11) is needed. It is possible to rewrite the input field as

$$\Omega = (|\Omega_l| + \Omega_r e^{-i\delta' t} + \Omega_b e^{i\delta' t})e^{i\Phi}, \tag{24}$$

where only one pair of sidebands have been included. In principle, there should be a sum over all possible δ', but for notational convenience this will be ignored.

The Doppler distribution in Eq. (23) has the following form:

$$W(\nu) = \frac{1}{\sqrt{2\pi}\sigma_\nu}\exp\left(\frac{-\nu^2}{2\sigma_\nu^2}\right), \tag{25}$$

where σ_ν is related to the FWHM of the Doppler profile via $\nu_{\mathrm{FWHM}} = (\sqrt{2\ln 2}/\pi)\sigma_\nu$. Note that ν_{FWHM} is measured in cycles per second (Hz) and σ_ν is measured in radians per second (s^{-1}). After evaluating the Doppler averaging a Doppler time scale is evident, is of the form

$$\tau_D = \sqrt{2}\left(\frac{\mathcal{R}}{\sigma_\nu \Delta}\right). \tag{26}$$

Typical experimental values result in $\tau_D \leqslant 0.55$ ns. If the coefficients A and B are considered slowly varying on a Doppler averaging time scale, a formal solution of Eq. (21) with the inclusion of Doppler averaging may be written as

$$\overline{\sigma}^{(1)} \approx e^{-i\delta' t}(A\Omega_r + B\Omega_b^*)\int_0^\infty \exp-\left(\frac{\sigma_\nu^2\Delta^2}{2\mathcal{R}^2}\tau^2+[a+i(\mathcal{R}-\delta')]\tau\right)d\tau + e^{i\delta' t}(A\Omega_b+B\Omega_\tau^*)\int_0^\infty \exp-\left(\frac{\sigma_\nu^2\Delta^2}{2\mathcal{R}^2}\tau^2+[a+i(\mathcal{R}+\delta')]\tau\right)d\tau. \tag{27}$$

The integrals in Eq. (27) can be expressed in terms of the complex error function as

$$I(\mathcal{A},\mathcal{B}_\pm)=\int_0^\infty e^{-(\mathcal{A}\tau^2+2\mathcal{B}_\pm\tau)}d\tau, \tag{28a}$$

$$=\frac{e^{\mathcal{B}_\pm^2/\mathcal{A}}\sqrt{\pi}\left[1-\mathrm{erf}\left(\frac{\mathcal{B}_\pm}{\sqrt{\mathcal{A}}}\right)\right]}{2\sqrt{\mathcal{A}}}, \tag{28b}$$

$$=\int_{-\infty}^{\infty}W(\nu)\frac{1}{a+i\left(\mathcal{R}\pm\delta'+\nu\frac{\Delta}{\mathcal{R}}\right)}d\nu, \tag{28c}$$

where

$$\mathcal{A}=\frac{\sigma_\nu^2\Delta^2}{2\mathcal{R}^2}, \tag{29a}$$

$$\mathcal{B}_\pm=\frac{1}{2}[a+i(\mathcal{R}\pm\delta')]. \tag{29b}$$

It can be shown that $I(\mathcal{A},\mathcal{B}_+)\ll I(\mathcal{A},\mathcal{B}_-)$, so terms containing $I(\mathcal{A},\mathcal{B}_+)$ will be dropped. After inverting Eqs. (15a) and (15b), the expression for $\sigma^{(1)}$ and $(\sigma^{(1)})^*$ may be substituted into Eq. (9) along with Eq. (24). The sideband equations of motion are found by collecting terms that oscillate at the red and blue sideband frequencies and by making the following transformations: $\Omega_r e^{i\Phi}\rightarrow\Omega_r$ and $\Omega_b e^{i\Phi}\rightarrow\Omega_b$, to produce a more familiar form. The equations of motion for the red and blue sidebands are as follows:

$$\frac{\partial\Omega_r}{\partial\zeta}=-i\nabla_\perp^2\Omega_r-\overline{\alpha_r}\Omega_r+\overline{\chi_{rb}}\Omega_b^*e^{-2i\Phi}, \tag{30a}$$

$$\frac{\partial\Omega_b}{\partial\zeta}=-i\nabla_\perp^2\Omega_b-\overline{\alpha_b}\Omega_b+\overline{\chi_{br}}\Omega_r^*e^{-2i\Phi}, \tag{30b}$$

where

$$\overline{\alpha_r}=-|\Delta_0|b_1^2\left(b_1^2\mathcal{D}-\frac{|\Omega_l|}{\mathcal{R}(r)}\sigma\right)I(\mathcal{A},\mathcal{B}_-), \tag{31a}$$

$$\overline{\alpha_b}=|\Delta_0|b_2^2\left(b_2^2\mathcal{D}+\frac{|\Omega_l|}{\mathcal{R}(r)}\sigma^*\right)I(\mathcal{A},\mathcal{B}_-)^*, \tag{31b}$$

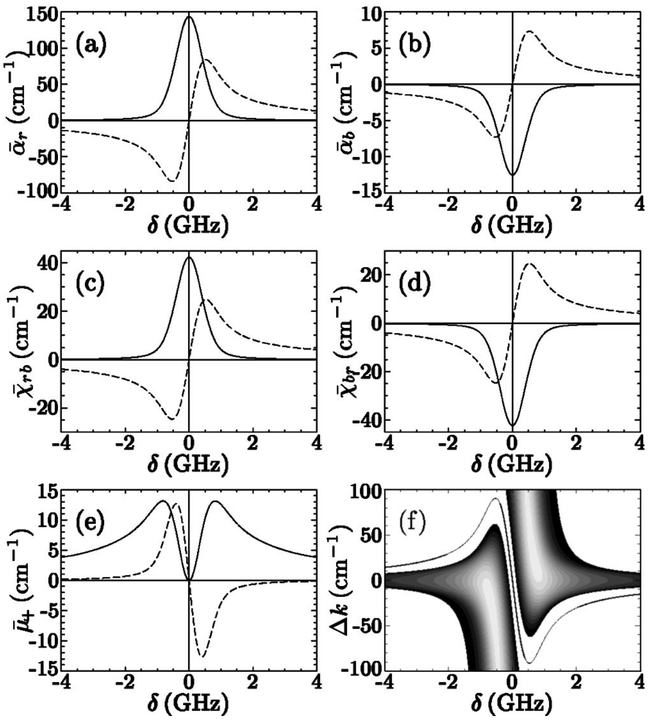

FIG. 2. Coupling coefficients of Eqs. (36a) and (36b). In plots (a) through (e) the solid line is the real part and the dashed line is the imaginary part. The input parameters are $\Omega_0=327.4$ GHz, $\Delta_0=212.3$ GHz, $\mathcal{R}_0=390.3$ GHz, $\Gamma/\gamma=6.6$, $N=1.0\times10^{14}$ cm^{-3}, and $\Delta k=0$ cm^{-1}. Plot (f) is a contour plot of Re$[\overline{\mu_+}]$ as a function of Δk and δ, with lighter shading representing larger values and ~ 0 outside the shaded region. The solid line on plot (f) is a plot of $\Delta k_z(\delta)$.

$$\overline{\chi_{rb}}=-|\Delta_0|b_1^2\left(b_2^2\mathcal{D}+\frac{|\Omega_l|}{\mathcal{R}(r)}\sigma\right)I(\mathcal{A},\mathcal{B}_-), \tag{31c}$$

$$\overline{\chi_{br}}=|\Delta_0|b_2^2\left(b_1^2\mathcal{D}-\frac{|\Omega_l|}{\mathcal{R}(r)}\sigma^*\right)I(\mathcal{A},\mathcal{B}_-)^*. \tag{31d}$$

In these expressions for the $\overline{\alpha}$'s and $\overline{\chi}$'s, the first-order solutions to $\mathcal{D}$ and σ have had the superscript (0) dropped. For the case of no Doppler averaging, the integral $I(\mathcal{A},\mathcal{B}_-)$ is replaced by a "resonant denominator," such that α_r has the following form:

$$\alpha_r=-|\Delta_0|b_1^2\frac{\left(b_1^2\mathcal{D}-\frac{|\Omega_l|}{\mathcal{R}(r)}\sigma\right)}{a+i[\mathcal{R}(r)-\mathcal{R}_0-\delta]}, \tag{32}$$

where the radial dependence of $\mathcal{R}$ is now shown explicitly. The generalized Rabi frequency $\mathcal{R}_0$ is used as a reference and is defined as $\mathcal{R}_0=\sqrt{\Omega_0^2+\Delta_0^2}$, where Ω_0 is defined as the on-axis $(\tilde{r}=0)$ Rabi frequency at $z=0$. The frequency dependence of Eqs. (31a) through (31d) about $\mathcal{R}_0$ are shown in Fig. 2 for the special case of solving Eqs. (18a) and (18b) in steady state. After removing diffraction, solving Eq. (18a) in steady state, and not including Doppler averaging $(\mathcal{A}=0)$, Eqs. (30a) and (30b) simplify the plane-wave sideband equations calculated by Boyd *et al.* [30] and Meystre and Sargent [31] with terms of order $(\gamma/\mathcal{R})^2$ dropped.

C. Calculation of the experimental observable

The far-field distribution of the field emerging from the exit plane has the following form:

$$\begin{aligned}\Omega(\theta,t)=\Omega_l(\theta,t)&+\sum_n a_n\Omega_{r,n}(\theta,t)e^{-i(\mathcal{R}_0+\delta_n)t}\\&+\sum_n a_n\Omega'_{b,n}(\theta,t)e^{i(\mathcal{R}_0+\delta_n)t}\\&+\sum_n b_n\Omega_{b,n}(\theta,t)e^{i(\mathcal{R}_0+\delta_n)t}\\&+\sum_n b_n\Omega'_{r,n}(\theta,t)e^{-i(\mathcal{R}_0+\delta_n)t}.\end{aligned}\tag{33}$$

The $\Omega'_{r,n}$ field is generated via coupling with the blue field, and the $\Omega'_{b,n}$ field is generated via coupling with the red field. The radial dependence of the fields has been converted to an angular (θ) dependence via a Hankel transform or, in the case of noncylindrical symmetry, a Fourier transform. The functions $\Omega(\theta,t)$ are slowly varying envelope functions. The fast oscillations and stochastic nature of the fields are contained in the $e^{\pm i(\mathcal{R}_0+\delta_n)t}$ term and the a_n's and b_n's respectively.

Following Eberly and Wodkiewicz [36], it is possible to calculate a time-dependent spectrum using a filtered field. By using appropriate frequency widths, derived from experimental and theoretical insights for the parameters involved in calculating the intensity spectrum one arrives at the following expression for the intensity spectrum:

$$\begin{aligned}I(\theta,\omega_d)\approx{}&\frac{\Gamma_d^2}{\Gamma_d^2+\omega_d^2}\int|\Omega_l(\theta,t)|^2dt+\sum_{\bar{n}}|a_{\bar{n}}|^2\frac{\Gamma_d^2}{\Gamma_d^2+[\omega_d+(\mathcal{R}_0+\delta_{\bar{n}})]^2}\int|\Omega_{r,\bar{n}}(\theta,t)|^2dt\\&+\sum_{\bar{n}}|b_{\bar{n}}|^2\frac{\Gamma_d^2}{\Gamma_d^2+[\omega_d-(\mathcal{R}_0+\delta_{\bar{n}})]^2}\int|\Omega_{b,\bar{n}}(\theta,t)|^2dt+\sum_{\bar{n}}|a_{\bar{n}}|^2\frac{\Gamma_d^2}{\Gamma_d^2+[\omega_d-(\mathcal{R}_0+\delta_{\bar{n}})]^2}\int|\Omega'_{b,\bar{n}}(\theta,t)|^2dt\\&+\sum_{\bar{n}}|b_{\bar{n}}|^2\frac{\Gamma_d^2}{\Gamma_d^2+[\omega_d+(\mathcal{R}_0+\delta_{\bar{n}})]^2}\int|\Omega'_{r,\bar{n}}(\theta,t)|^2dt\\&+2\,\mathrm{Re}\left[\sum_{\bar{n}}a^*_{\bar{n}}b_{\bar{n}}\frac{\Gamma_d^2}{\Gamma_d^2+[\omega_d+(\mathcal{R}_0+\delta_{\bar{n}})]^2}\int\Omega^*_{r,\bar{n}}(\theta,t)\Omega'_{r,\bar{n}}(\theta,t)dt\right]\\&+2\,\mathrm{Re}\left[\sum_{\bar{n}}b^*_{\bar{n}}a_{\bar{n}}\frac{\Gamma_d^2}{\Gamma_d^2+[\omega_d-(\mathcal{R}_0+\delta_{\bar{n}})]^2}\int\Omega^*_{b,\bar{n}}(\theta,t)\Omega'_{b,\bar{n}}(\theta,t)dt\right].\end{aligned}\tag{34}$$

A complete description of the approximations used in the derivation of Eq. (34) is given in the thesis of Paul [35]. The index n of Eq. (33) has been replaced with $\bar{n}$ in equation Eq. (34). As a result of the resolution width of the detector (Γ_d), the infinitesimally spaced modes of Eq. (33) are replaced with the resolvable modes of Eq. (34). The resolution width of the detector sets the spacing of the $\delta_{\bar{n}}$'s needed to reproduce experimental spectra.

As a result of the work done by You *et al.* [34] we are able to completely separate the physics of seeding the sidebands from the propagation and gain of the sidebands. Of course, the final observable is dependent on the form of the input seed as shown in Eq. (34) by the inclusion of the appropriate $a_{\bar{n}}$'s and $b_{\bar{n}}$'s coefficients. In this paper our main concern is the propagation properties of Eqs. (30a) and (30b), the equations of motion for the sidebands.

III. COMPUTATIONAL RESULTS

In general a full solution would consist of solving Eqs. (18a), (19), (30a), and (30b) self-consistently. This could be done by first solving Eqs. (18a) and (19) at a given time step (t_i) resulting in $\mathcal{D}(x,y,z,t_i)$, $\sigma(x,y,z,t_i)$, and $\Omega_l(x,y,z,t_i)$ at every grid point. This information can then be used to solve Eqs. (30a) and (30b) for a given $\delta_{\bar{n}}$; once for a red input seed and once for a blue input seed. The sideband propagation is then repeated for all of the $\delta_{\bar{n}}$'s in question. At the end of a given time step the following fields should be saved for further analysis: $\Omega_l(x,y,z_{\mathrm{exit}},t_i)$, $\Omega_{r,\bar{n}}(x,y,z_{\mathrm{exit}},t_i)$, $\Omega'_{r,\bar{n}}(x,y,z_{\mathrm{exit}},t_i)$, $\Omega_{b,\bar{n}}(x,y,z_{\mathrm{exit}},t_i)$, and $\Omega'_{b,\bar{n}}(x,y,z_{\mathrm{exit}},t_i)$. At the end of this time-dependent calculation the saved fields may be placed into Eq. (34) with the appropriate values for the coefficients $a_{\bar{n}}$ and $b_{\bar{n}}$ to model the input statistics in question. Even though many computational time-saving simplifications have been made in deriving the equations of motion, a full time-dependent calculation is still not feasible with available facilities; only steady-state solutions will be presented.

In the following a plane-wave solution with an effective diffraction will be presented, which will give valuable insight for a more complete calculation. Steady-state solutions to Eqs. (18a), (19), (30a), and (30b) with cylindrically symmetric input seeds will be presented. It will be shown that at this level of approximations the sidebands do not experience significant gain. Finally, possible explanations will be given to account for the lack of significant predicted gain.

A. Plane-wave solutions

Solving Eq. (18a) in steady state allows the evaluation of the $\overline{\alpha}$'s and $\overline{\chi}$'s in steady state. After neglecting diffraction and assuming the laser is not attenuated during propagation the following solution for the laser propagation may be written down:

$$\Omega_l(\zeta) \approx \Omega_0 e^{-ik_l\zeta}, \tag{35}$$

where $k_l = \mathrm{Im}[\overline{\alpha_l}]$. With similar definitions for $k_r = \mathrm{Im}[\overline{\alpha_r}]$ and $k_b = \mathrm{Im}[\overline{\alpha_b}]$, the quantities $\Delta k_z = 2k_l - k_r - k_b$ and $\Delta k = \Delta k_z + \Delta k_\nabla$, where Δk_∇ is an assumed additional effective phase resulting from diffraction, may be used to rewrite the sideband Eqs. (30a) and (30b) as

$$\frac{\partial \Omega_r}{\partial \zeta} = -(\mathrm{Re}[\overline{\alpha_r}] - i\Delta k)\Omega_r + \overline{\chi_{rb}}\Omega_b^*, \tag{36a}$$

$$\frac{\partial \Omega_b^*}{\partial \zeta} = -\mathrm{Re}[\overline{\alpha_b}]\Omega_b^* + \overline{\chi_{br}^*}\Omega_r. \tag{36b}$$

The parameter Δk is considered to be an adjustable parameter that can be varied to maximize the gain of the sidebands. The justification for this is that when diffraction is included spatial-dependent phase variations will arise, effectively sampling all Δk values resulting in those with large gain being observed.

The solution to Eqs. (36a) and (36b) has the form (for $i = 1, 2$)

$$\Omega_i = C_{1,i} e^{\overline{\mu_+}\zeta} + C_{2,i} e^{\overline{\mu_-}\zeta}, \tag{37}$$

where

$$\overline{\mu_\pm} = \frac{1}{2}[-(\mathrm{Re}[\overline{\alpha_b}] + \mathrm{Re}[\overline{\alpha_r}] - i\Delta k) \pm \sqrt{\beta}], \tag{38}$$

and

$$\beta = (\mathrm{Re}[\overline{\alpha_r}] - i\Delta k - \mathrm{Re}[\overline{\alpha_b}])^2 + 4\overline{\chi_{br}^*}\,\overline{\chi_{rb}}. \tag{39}$$

The $\overline{\mu_-}$ term is responsible for transient behavior near $\zeta = 0$ and in general is not of interest for long cell lengths ($z > -8\pi|\Delta_0|/(3\,\mathrm{Re}[\overline{\mu_-}]N\lambda^2\Gamma)$). The $\overline{\mu_+}$ term is responsible for the gain of the sidebands. A plot of $\overline{\mu_+}$ for typical experimental values is shown in part (e) of Fig. 2. Part (f) of Fig. 2 is a contour plot of $\mathrm{Re}[\overline{\mu_+}]$ versus Δk and δ. The parameter Δk_z is a function of δ and is the special case of Δk with no additional phase added to simulate diffraction, i.e., $\Delta k_\nabla = 0$. When $\Delta k = \Delta k_z$, all three waves, the laser, and the two sidebands are colinear, and the two sidebands experience loss ($\mathrm{Re}[\overline{\mu_+}(\Delta k_z)] < 0$). If the sidebands do experience gain ($\mathrm{Re}[\overline{\mu_+}] > 0$), the output intensity of the blue sideband is always greater than the output intensity of the red sideband for long propagation lengths and blue laser detuning, regardless of the initial conditions of the red and blue sidebands. This results from the lower atomic absorption at the blue detuning.

The plane-wave calculations presented here are very similar to Boyd *et al.* [30], with the difference being that we have included Doppler averaging and made approximations such that $\Delta_0 \gg \gamma$ must be satisfied. In the theory of ours and Boyd *et al.* the shape of the gain profile is the same and the blue sideband intensity is always predicted to be greater than the red sideband intensity for long propagation lengths.

With expressions for k_l, k_r, and k_b it is possible to formulate a simple expression for the angle of the conical emission at the red sideband. Many different physical models have been presented (see Ref. [26] for a short overview of many different models), all with the same basic result:

$$\theta_c = \frac{k}{\sqrt{8\pi}}\sqrt{3\lambda^3\Gamma}\sqrt{N/\Delta_0}, \tag{40}$$

where θ_c is the cone half-angle and k is a dimensionless constant of proportionality (of order unity) that varies between different theories. This cone angle is the angle of the peak intensity of the frequency integrated red sideband.

The α_c model

One of the shortcomings of a plane-wave model, when compared to experiment, is that it predicts that the coherently propagating sidebands always have more blue intensity than red. This observation is consistent with what is known about the power spectrum of light scattered by two-level systems: the Mollow spectrum [37]. The red sideband in our case, or more generally the sideband closest to the atomic resonance, will experience a greater amount of incoherent scattering. This fact results in the sideband closest to resonance having greater intensity in the Mollow scattering spectrum. For coherent propagation along the axis, the opposite must be true. However, in the experiment more red detuned cone light is seen than blue detuned on-axis light; see Refs. [19] and [22]. In the α_c model, we apply a plane-wave calculation to an imagined filament with coherent loss from the on-axis red-detuned sideband. This loss is added coherently to form a forward direction red cone.

Imagine a single self-focused filament, which has written a radially varying index of refraction $[n(r,\omega)]$ in the medium to produce self-focusing. It might also be possible for this $n(r,\omega)$ to confine the blue sideband via internal reflection, since $n(r,\omega)$ decreases with increasing r. The red sideband, on the other side of the resonance, would not be trapped and would leak out of the filament region. This red sideband light that is leaking out of the filament is coherent and does not contribute to the 4π incoherent scattered light. If the spatial rate at which this coherent light leaks out of the filament region is denoted by α_c it is possible to add up this light coherently to form a cone. This model results in the following equations of motion:

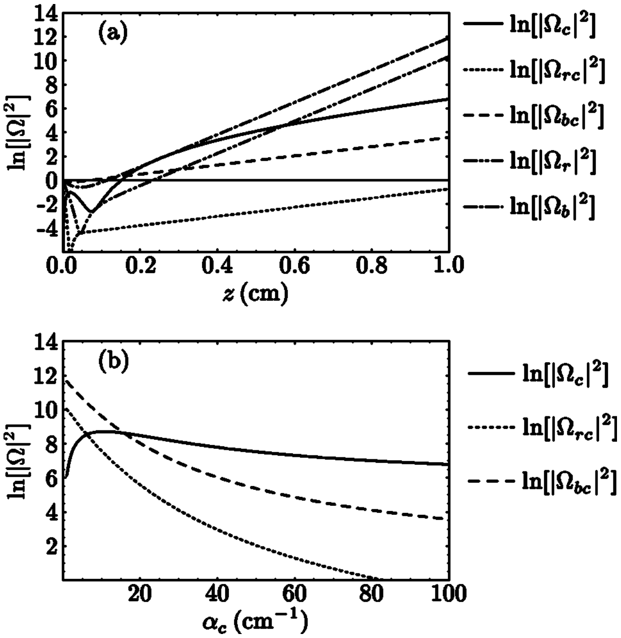

FIG. 3. Solutions to Eqs. (41a) through (41c) and Eqs. (36a) and (36b) are shown in plot (a) with $\alpha_c = 100\ \mathrm{cm}^{-1}$. The quantities $|\Omega_c|^2$, $|\Omega_{rc}|^2$, and $|\Omega_{rc}|^2$ are the intensities in the cone, on-axis red sideband and on-axis blue sideband, respectively. The quantities $|\Omega_r|^2$ and $|\Omega_b|^2$ are the intensities of the on-axis red and blue sidebands in the absence of a cone ($\alpha_c = 0$). Plot (b) shows the intensity of the cone and the two on-axis sidebands at the end of a 1 cm propagation, as a function of α_c.

$$\frac{\partial \Omega_c}{\partial \zeta} = \alpha_c \Omega_{rc}, \tag{41a}$$

$$\frac{\partial \Omega_{rc}}{\partial \zeta} = -(\mathrm{Re}[\overline{\alpha}_r] - i\Delta k + \alpha_c)\Omega_{rc} + \overline{\chi}_{rb}\Omega_{bc}^*, \tag{41b}$$

$$\frac{\partial \Omega_{bc}^*}{\partial \zeta} = -\mathrm{Re}[\overline{\alpha}_b]\Omega_{bc}^* + \overline{\chi}_{br}^*\Omega_{rc}, \tag{41c}$$

where Ω_c is the amplitude of the red light that leaks out of the filament and is added up to produce the cone; Ω_{rc} and Ω_{bc} are the red and blue sideband fields, respectively, that are within the filament.

Solutions to Eqs. (41a) through (41c) are presented in Fig. 3. Both sideband input fields are given the same magnitude of 1 with a relative phase difference of $3\pi/2$. (The initial phase difference is inconsequential for large propagation distances.) For comparison, the solutions to the normal plane-wave equations [Eqs. (36a) and (36b)] are shown. The intensity of the cone and the two on-axis sidebands at the end of a 1 cm propagation, as a function of α_c is also shown.

Upon solving Eqs. (41a) through (41c), it is evident that the red intensity within the filament ($|\Omega_{rc}|^2$) is always less than the blue intensity ($|\Omega_{bc}|^2$), as seen in Fig. 3. The reason is the same as before: the incoherent scattering is greater for the red than the blue sideband, whereas the cone light is coherent loss from the red field in the imagined filament. In the limit of large α_c the red sideband in the filament is lost to the red sideband in the cone such that the feedback to the blue sideband in the filament through the $\overline{\chi}_{br}^*$ coefficient is reduced to the point that the blue sideband can only experience three-photon gain. The interaction between the laser and the blue sideband produces red sideband light via $\overline{\chi}_{rb}$ in Eq. (41b), which is lost to the cone. The most important result of this model is that for large values of α_c ($\alpha_c > 20\ \mathrm{cm}^{-1}$ for the conditions used for Fig. 2 along with $\delta = 1.5$ GHz), the intensity in the red cone is greater than the intensity of the on-axis blue sideband. This prediction is in agreement with experiment, in contrast with the prediction of the plane-wave model. We present this model for the purpose of illustrating the large impact that diffraction and transverse propagation can have on the gain dynamics.

B. Steady-state cylindrically symmetric solutions with diffraction

In this section, Eq. (19) for the pump field will be solved numerically in steady state. This seemingly simple equation is the subject of many articles [32,38–43]. However, our main concern is the impact of the pump behavior on the propagation of the red- and blue-detuned sidebands, in Eqs. (30a) and (30b). The figures presented in this section will be for the propagation of one set of parameters that result in single-filament laser propagation. These parameters are also within the range for our experimental conditions [22], and have been observed to produce reasonably stable propagation in z. The experimental parameters used for this propagation correspond to the point $\{\Phi/\Phi_K, \rho_{1/2}\} = \{40.0, 2.57\}$ in a dimensionless self-focusing space [22,32]. All propagations are for strontium vapor with resonance line wavelength $\lambda = 460.377$ nm. A contour plot of this laser propagation is shown in Fig. 4. This propagation yields nearly constant beam diameter through the vapor. The radial shape of the input beam is Gaussian, which does not match the stationary filament solution. As a result a Gaussian beam will always have oscillations in its diameter while propagating [32]. Parts (a) and (b) show a contour plot of $|\Omega_l(\tilde{r},z)|^2$ and $\tilde{r}|\Omega_l(\tilde{r},z)|^2$, respectively, with linearly spaced contour lines. Parts (c) and (d) show these with logarithmically spaced contour lines, each a factor of $\sqrt{2}$ below the previous line. The main part of the self-focusing occurs between the horizontal dotted lines at $z = 0$ cm and $z = 5$ cm where the number density is constant. Before $z = 0$ cm and after $z = 5$ cm the number density smoothly drops to zero, similar to the experiment. The thick line on Fig. 4 is the $\tilde{r}_{1/2}$ line, which is a measure of the radius of the beam. The parameter $\tilde{r}_{1/2}$, which is the radius which contains half of the power (P) of the beam, is defined as

$$P = \int_0^\infty 2\pi r|\Omega(r)|^2 dr = 2\int_0^{\overline{r}_{1/2}} 2\pi r|\Omega(r)|^2 dr. \tag{42}$$

The dashed line is the $\tilde{r}_{1/2}$ line for free diffraction in the absence of the vapor.

Plot (a) of Fig. 4 most clearly displays the overall propagation of the laser filament, when the predominant effect is self-focusing. Plot (d) of Fig. 4 most clearly displays the

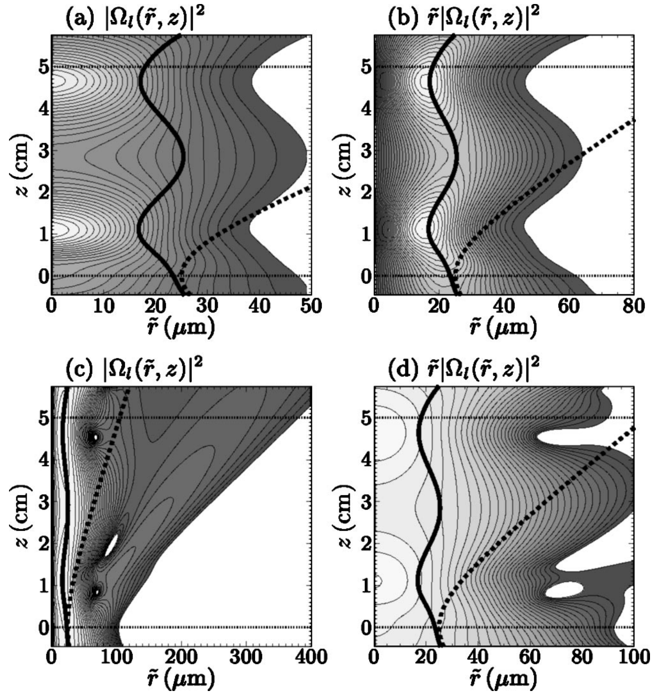

FIG. 4. Steady-state laser propagation. The free space input beam is a Gaussian with $\tilde{r}=25\ \mu$m and $\Omega_0=327.4$ GHz. Other input parameters are $\Delta_0=212.3$ GHz, $\mathcal{R}_0=390.3$ GHz, $\Gamma/\gamma=6.6$, and $N=1.0\times10^{14}\ \mathrm{cm}^{-3}$. Plots in the top row have linear contour lines, while the logarithmic contour lines in the bottom plots differ by a factor of $\sqrt{2}$. The left columns are plots of $|\Omega_l(\tilde{r},z)|^2$, while the right columns are plots of $\tilde{r}|\Omega_l(\tilde{r},z)|^2$. The number density is a constant from $z=0-5$ cm; before $z=0$ cm and after $z=5$ cm, it smoothly drops to zero. The thick line is the $\tilde{r}_{1/2}$ of the laser as a function of z. The dashed line is the $\tilde{r}_{1/2}$ for free diffraction.

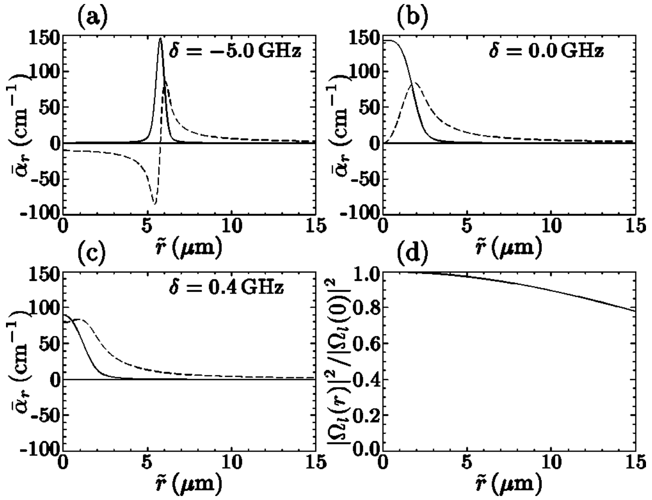

FIG. 5. Radial dependence of α_r is shown in plots (a)–(c) for the Gaussian laser beam shown in plot (d). The four-wave interaction region is centered about the maximum of $|\alpha_r|^2$. The solid line is Re$[\alpha_r]$, and the dashed line is Im$[\alpha_r]$.

laser intensity at large $\tilde{r}$. Although clear evidence of self-focusing is present in plot (d), it is also possible to observe the propagation of the low-intensity laser wings. To emphasize CE angles, contour plots of the sidebands will be presented in the form of plot (d) of Fig. 4.

The coupling coefficients ($\overline{\alpha}$'s and $\overline{\chi}$'s), which are functions of $|\Omega_l|^2$, are now functions of $\tilde{r}$ and z, because $|\Omega_l|^2$ is a function of $\tilde{r}$ and z. Plots of $\alpha_r(\tilde{r})$ are shown in parts (a)–(c) of Fig. 5 for a Gaussian laser beam and different values of δ. In each plot the solid line is Re$[\alpha_r(\tilde{r})]$ and the dashed line is Im$[\alpha_r(\tilde{r})]$. Part (d) of Fig. 5 is the normalized Gaussian laser profile that was used to produce plots (a)–(c). Here the Re$[\alpha_r(\tilde{r})]$ peaks occurs when the denominator of Eq. (32) is a minimum. Note that this resonance condition covers a small range in $|\Omega_l|^2$, hence a small $\Delta\tilde{r}$ range. As a result, large sideband gain occurs in a small fraction of the beam area for a given sideband detuning.

With the addition of diffraction, even in the simplest case of cylindrical symmetry, the sideband propagation problem becomes much more complicated. Each of the coupling coefficients in Eqs. (30a) and (30b) has a maximum or minimum, where $|\alpha_r(\tilde{r})|$ is a maximum. Within some range, $\Delta\tilde{r}$ around this maximum is the optimal interaction region where the majority of four-wave mixing can take place if the condition of appropriate phase matching is present. Within a single filament an optimal interaction region for a given set of sidebands (a given value of δ) will be a ring that will vary in radius during the propagation in z. It is important to notice that the entire optimal interaction region is within only ~5% change in the laser intensity, as can be seen by looking at plots (a) and (d) of Fig. 5. Visualizing the propagation of the sidebands is further complicated by the propagation of the laser. The radial shape of the laser will vary, changing the shape, $\tilde{r}$ location, and width of the optimal interaction region. As a result of the coupling coefficients being a function of $|\Omega_l|^2$, the optimal interaction region for a given δ will follow one of the contour lines of plots (a) or (c) of Fig. 4. It is important to notice that there are values of δ that will produce an interaction region that will propagate with nearly constant radius, as do some of the contour lines of plots (a) and (c) of Fig. 4. Also there are values of δ that will produce an interaction region which will come in and out of existence during laser propagation, as do some of the contour lines of plots (a) and (c) of Fig. 4.

The optimal interaction region is influenced by many parameters. The value of δ, which is referenced to the generalized Rabi frequency ($\mathcal{R}_0$) at $z=0$ and $\tilde{r}=0$, determines where in $\tilde{r}$ the optimal interaction region is located. If $\delta<0$ then the optimal interaction region is away from the origin. The more negative δ becomes, the farther the optimal interaction region moves away from the origin. When $\delta>0$ only the tail of the optimal interaction region is present. The width of the optimal interaction region is effected by the radial intensity shape of the laser. As the laser propagates, the width, shape, and location of the optimal interaction region will change.

1. Propagation results

The experimental observable is outlined in Eq. (34). As a result of considering only steady state in this section, the time integrals may be ignored. All that will be presented will be the field terms in the summations of Eq. (34). This is a

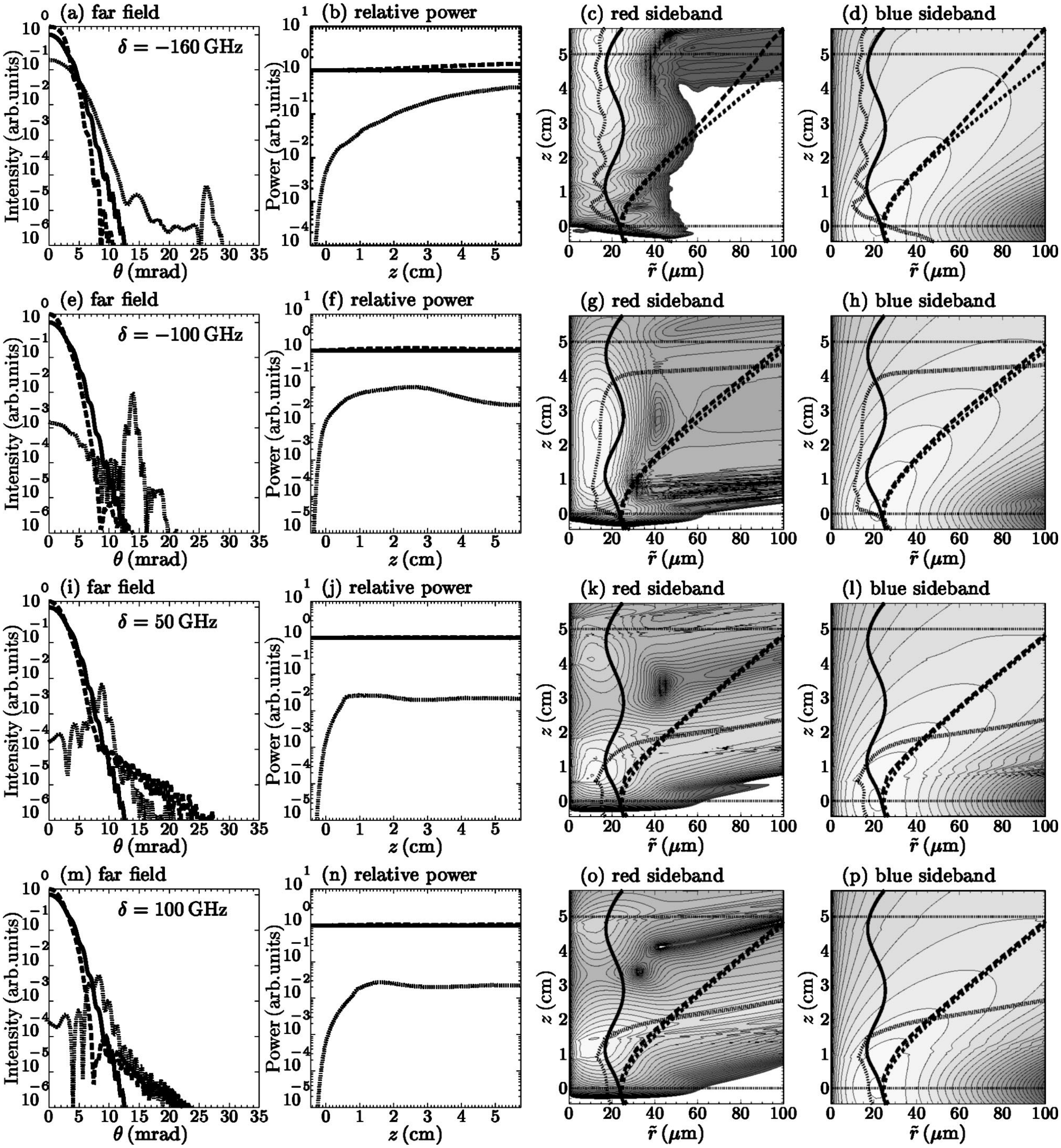

FIG. 6. Four sideband propagations with a blue-detuned input seed. Each row is a different propagation with δ shown in the left-column plot. In each plot the laser is denoted with a solid line, the blue sideband with a long-dashed line, and the red sideband with a dotted line. The left column is the far field scaled to the input laser power. The second column is the power in the fields as a function of z, scaled to the input laser power. The right two columns are logarithmic contour plots of $\tilde{r}|\Omega_r|^2$ and $\tilde{r}|\Omega_b|^2$ for the red and blue sidebands, respectively. Each of the contour plots displays the $\tilde{r}_{1/2}$ lines for each of the fields and for free diffraction. The $\tilde{r}_{1/2}$ for free diffraction is denoted with a short-dashed line. (Laser, solid line; free diffraction, short-dashed line; blue sideband, long-dashed line; red sideband, dotted line.)

reasonable representation of the calculations because our main concern is to investigate the gain and propagation properties of the sidebands.

Description of plots. Two sets of sideband propagations are presented in Figs. 6 and 7, using the laser propagation shown in Fig. 4 with a blue and red seed, respectively. The laser and sideband input at $z = -0.45$ cm is calculated such that free space propagation to $z = 0$ cm will produce a Gaussian with flat phase front and width of 50 μm FWHM ($\tilde{r}_{1/2} = 25$ μm). This corresponds to what was done in the experiment [22]. All the plots in Fig. 6 are for a blue input seed. Four seed-frequency simulations, with the δ values shown on

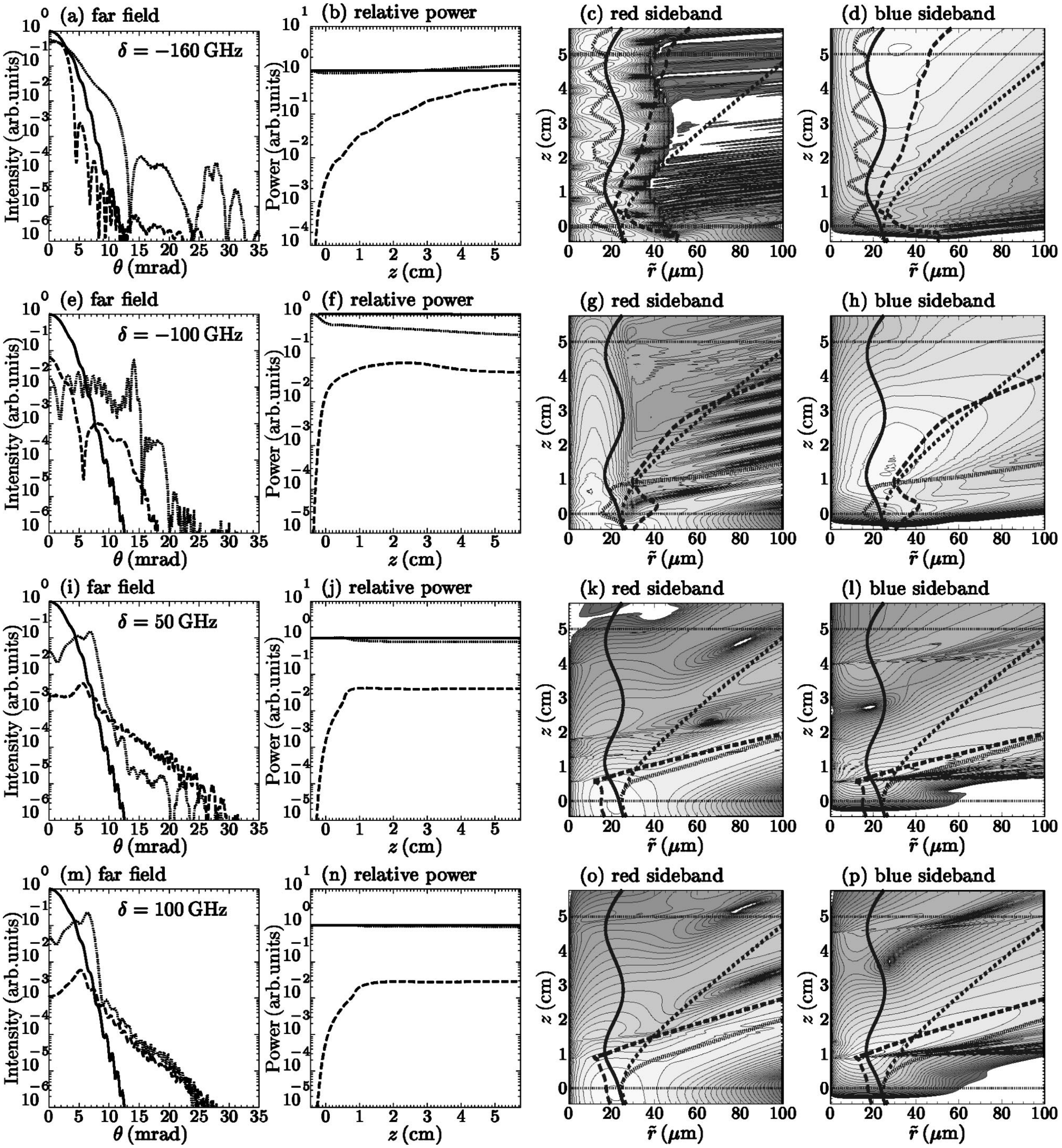

FIG. 7. Four sideband propagations with a red input seed. All of the plots and symbols are the same as in Fig. 6.

the plots, correspond to the four rows of Fig. 6. (The definition of δ is presented in Fig. 1.) Note, that the values of δ in Figs. 6 and 7 are much larger than in the previous examples. This is a result of how δ is defined. δ is a relative detuning from the on-axis generalized Rabi frequency of the input laser at the entrance of the medium. As the laser propagates, the on-axis and radial values of the generalized Rabi frequency varies over a large range (see Fig. 1). This variation results in the optimal interaction region being produced for a wide range of δ values. The left column shows the far fields of the laser, and the two sidebands, with the input seed scaled to the input laser power. The far field of the laser is the same in each plot. The laser is slightly wider than would be expected for the free diffraction of a 50 μm FWHM spot because when the laser exits the self-focusing region of the cell ($z = 5$ cm), it is smaller than 50 μm FWHM. The second column shows the relative power in the laser and the two sidebands; the loss in laser power during propagation is not noticeable in these graphs. In the calculations presented, the only mechanism for laser attenuation comes from absorption, as seen in Eq. (20). The two columns on the right are contour plots with logarithmic ($\sqrt{2}$ ratio) contour lines of $\tilde{r}|\Omega_r|^2$ and

$\tilde{r}|\Omega_b|^2$, respectively, as in plot (d) of Fig. 4 for the laser. In this type of plot it is easy to follow low-intensity light at large $\tilde{r}$. On each one of the contour plots are the $\tilde{r}_{1/2}$ lines for each of the fields and for free diffraction. The layout of Fig. 7 is the same as Fig. 6.

Numerical method. A Crank-Nicholson method is used to propagate the laser and the sidebands [44]. The singularity resulting from the Laplacian in cylindrical coordinates at the origin is dealt with by methods described by Drummond [45]. All the functions relevant to the propagation are evaluated on a radial grid with a higher concentration of data points near the origin than at large $\tilde{r}$. Only 1% of the data used in the calculations for Figs. 6 and 7 are used to produce the contour plots.

Sideband propagation. The influence of the optimal interaction region, discussed in Sec. III B, can be seen on plot (c) of Figs. 6 and 7. Both plots of the red sideband show a sharp cut-off in intensity that approximately follows the last laser contour line of plot (a) of Fig. 4. This optimal interaction region is able to produce a radially dependent "index of refraction" $[n(\tilde{r})]$ that is capable of trapping the red sideband. This trapping is seen again in plot (g) of both figures. Here, "index of refraction" was placed in quotes because it is not a well-defined quantity. There are two levels of estimating the "index of refraction." The first is the standard dispersion line shape of the unexcited vapor, which with increasing saturation approaches the vacuum value. This suggests that the red sideband should be refracted out of the filament and the blue sideband should be partially or fully held within the filament via internal reflection [27]. By looking at the right two columns of Figs. 6 and 7 this is obviously not the case. A more descriptive index of refraction includes the atomic response at the sideband frequencies to the laser field, and it can be found by using $\mathrm{Im}[\alpha_r(\tilde{r})]$ for the red sideband and $\mathrm{Im}[\alpha_b(\tilde{r})]$ for the blue sideband. With this, one finds that the radial shape of $n(r)-1$ for the red sideband is the same as the dashed line in plots (a)–(c) of Fig. 5. The shape of $n(r)-1$ for the blue sideband is the same as the red, but it is one to two orders of magnitude smaller. (The relative size of α_r and α_b can be seen in Fig. 2.) Therefore, there is a trapping "index of refraction" for both the red and blue sidebands, but the index gradient is too small to confine the blue sideband. This interpretation of the index of refraction is useful, and it will be used to explain other observations. However, it should be kept in mind that when two waves are strongly coupled, as the red and blue sidebands are, an index of refraction is not a well-defined quantity.

For the propagations in the bottom two rows of Figs. 6 and 7, $\delta > 0$. This results in only the tail of the optimal interaction region being present at $z=0$. But in both cases the laser beam self-focused into an intensity that is great enough to bring the center of the optimal interaction region into existence. This happened in two places, once at $z\approx 1$ cm and then again at $z\approx 4.6$ cm. The result of this can best be seen in plots (l) and (p) of Fig. 7, and, with careful observation, evidence can be seen in plots (k), (l), (o), and (p) of both figures. When the center of the optimal interaction region comes in and out of existence rapidly in space, the requirements for phase matching between the red and blue sidebands also change rapidly in space. This results in sudden changes in gain and refraction. The sudden change in refraction is what is seen as sharp wiggles on the contour plots. The sudden change in gain can be seen in the generated field for the first appearance of the optimal interaction region in plots (j) and (n) of both Figs. 6 and 7. In plots (j) and (n) of Fig. 7, around $z=1$ cm a sudden jump in gain for the blue sideband is observed. The change in gain for the seeded field is not noticed except in plot (j) of Fig. 7 where, around $z=1$ cm, the red sideband experiences a sudden loss of power. There is no change in gain evident for the second location of the interaction region coming into existence around $z\approx 4.6$ cm. This is a result of the blue sideband diffracting out from the origin, leaving only a small relative intensity near the origin which will experience the gain.

In all eight propagations in Figs. 6 and 7, the generated field experiences strong gain before $z\approx 0.5$ cm, but never increases without bound, as is seen in the plane-wave calculations [30]. The initial rapid growth of the generated field results from the fact that it is created with the correct phase matching to experience gain. Once both fields start diffracting and the laser propagation moves the optimal interaction region to a new $\tilde{r}$, the requirements for phase matching change. This is not an issue in a plane-wave calculation. However, it is expected that there will be other locations where the conditions for phase matching will be met, and both sidebands will again experience large gain.

The fact that the blue sideband diffracts out of the optimal interaction region can be seen clearly with a blue seed in the plots in the right column of Fig. 6. Especially in plots (h), (l), and (p) the blue sideband $\tilde{r}_{1/2}$ line follows the free diffraction $\tilde{r}_{1/2}$ line. The only deviation from free diffraction is a result of small amounts of gain received in the optimal interaction region. This is seen in plots (b) and (d) of Fig. 6. Plot (b) shows the blue sideband that receives the most gain of all cases, and therefore the $\tilde{r}_{1/2}$ line on plot (d) is most influenced by this gain received in the optimal interaction region. The plots in the left column also show that the blue sideband is predominantly influenced by diffraction. Notice that the laser and the blue sideband have comparable far-field profiles.

The blue field generated by a red seed is also influenced by the optimal interaction region, as can be seen in the right column of Fig. 7. In each case, once the blue sideband is created it begins to diffract out of the optimal interaction region. Again in plot (d), the blue sideband $\tilde{r}_{1/2}$ line is slowed by the fact that the red sideband is trapped and is able to continue the production of blue light. The main difference between the propagations at $\delta=-160$ GHz and $\delta=-100$ GHz is that the incoherent scattering of red light is much less in the $\delta=-160$ GHz case. Even though the gain for blue light is initially greater for the $\delta=-100$ GHz case, the red light is lost to incoherent scattering as can be seen in plot (f), resulting in less over all gain in blue light for the $\delta=-100$ GHz case versus the $\delta=-160$ GHz. In plots (l) and (p), the blue light is suddenly refracted out at a steep angle as a result of the appearance of the optimal interaction region around $z=1$ cm. Notice that the far field of the blue sideband in plots (e), (i), and (m) of Fig. 7, and the far field

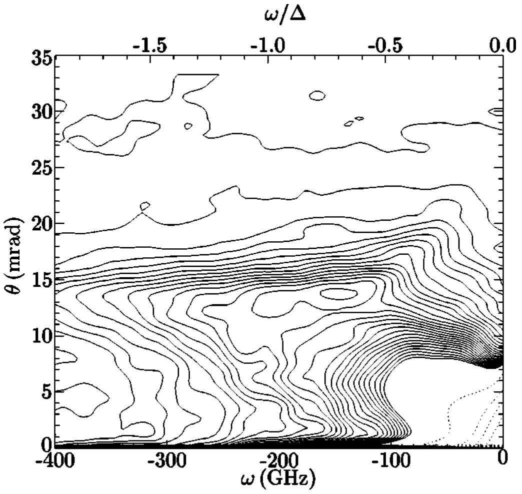

FIG. 8. Intensity distribution of an experimental cone. The experimental parameters for this cone are as follows: $\Delta = 210$ GHz, $\Gamma/\gamma = 6.6$, $N = 9.2\times 10^{13}$ cm^{-3}, input beam size 50 μm FWHM, and input laser energy 2.21 μJ. From these experimental parameters, $\Omega_0 = 331$ GHz, $\mathcal{R}_0 = 392$ GHz, and $\{\Phi/\Phi_K, \rho_{1/2}\} = \{38.6, 2.48\}$ can be estimated. The bottom axis is the frequency relative to the atomic line. The top axis is the frequency relative to the atomic line scaled by the laser detuning. The left axis is the emission angle. The peak of the cone intensity is at $\{\omega, \theta\} = \{-150$ GHz,13.5 mrad$\}$. The bottom right region shows the on-axis red light near the atomic line. The dashed contour lines in the extreme bottom right corner are spaced at ten times that of the solid lines, much of this is laser light scattered around the frequency block in the monochromator.

of the blue sideband in plots (e), (i), and (m) of Fig. 6, have a similar structure for $\theta > 5$ mrad. Especially in plot (e) of both figures a peak is seen at $\theta \approx 10$ mrad. This implies that the blue light that is generated via mixing with the red is sent out into high angles.

Cones. In all cases, in Figs. 6 and 7 the red sideband produces a cone. The most important observation for the red sideband propagation is the formation of a cone regardless of which sideband is seeded. This implies that both refraction and phase matching contribute to the formation of a red cone. In the case of a red seed refraction is the main cause of the calculated observed cones. As a result of the red sideband experiencing little relative gain only refraction is left to reshape the input seed into a cone. In the case of a blue seed, the red sideband is created with appropriate phase to be directed into a cone. Of course in both cases both effects are present, directing red light into a cone. This is not the case for the blue sideband. With a blue seed, the blue sideband undergoes virtually free diffraction, and with a red seed the blue sideband is in some cases phase matched into a weak cone as seen in plots (i) and (m) of Fig. 7.

Only for the case $\delta = -160$ GHz, [plot (a) in both Fig. 7 and Fig. 6] the largest red peak is on axis, not in a cone. This on-axis red light near the atomic transition is also seen in the experiment, as shown in Fig. 8. The angular width of the main peak of the red far-field pattern is wider than both the laser and blue sideband. This implies that the majority of the red sideband was confined inside of a filament smaller than the trapped laser beam. This is confirmed in plot (c) of Figs. 6 and 7.

(a) red cone; blue seed

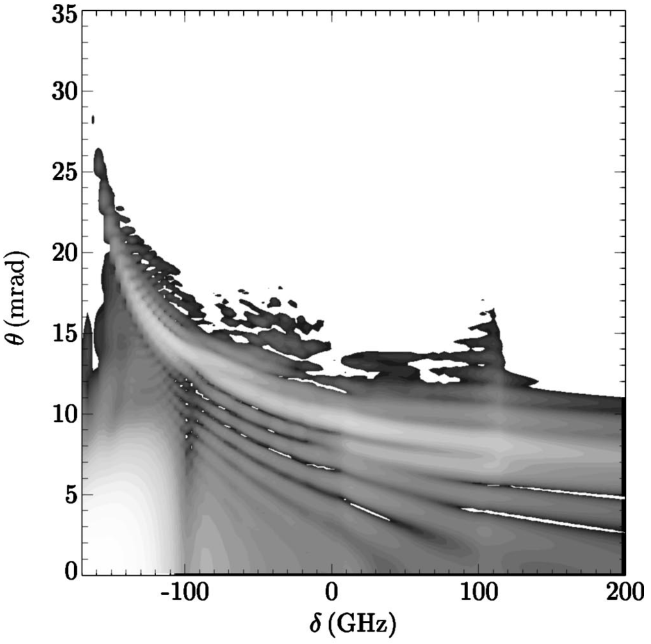

(b) red cone; red seed

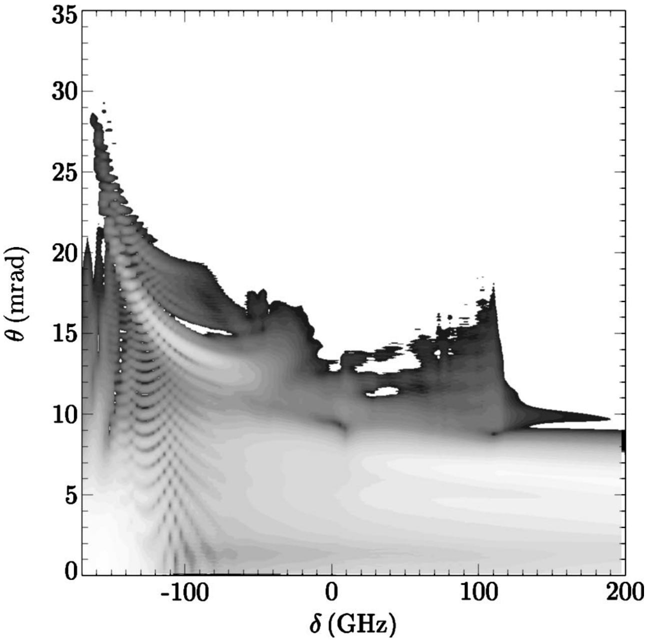

FIG. 9. A blue input seed was used for the simulation in plot (a). A red input seed was used for the simulation in plot (b). Both plots are logarithmic contour plots of the far field of the red sideband. Lighter regions represent greater intensity.

The theoretical shape of a cone is shown in Fig. 9. This is simply a contour plot with logarithmic levels of many far-field calculations for the red sideband, as shown in the left column of Figs. 6 and 7 for many values of δ, the detuning from $\mathcal{R}_0$. Plot (a) of Fig. 9 shows propagation results when a blue input seed is used; plot (b) is for a red seed. Plot (a) is the integrand of the fifth term in Eq. (34), where the δ axis

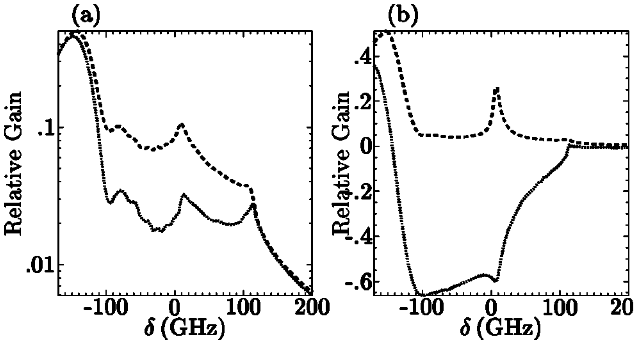

FIG. 10. A blue (red) input seed was used for the simulation in the left (right) column. Plots (a) and (b) show relative gain, which is defined in Eq. (43) for both the sidebands. The blue sideband is denoted by the dashed line and the red sideband is denoted by the dotted line.

corresponds to the $\overline{n}$ and the time integral is ignored because of the condition of steady state. Plot (b) is the integrand of the second term in Eq. (34).

The theoretical cones shown in Fig. 9 can be compared to the experimental cone in Fig. 8. The horizontal axis of Fig. 8 is detuning from the atomic line, while the horizontal axes in Fig. 9 are δ, which is detuning from $\mathcal{R}_0$. The conversion $\omega = \Delta_0 - \mathcal{R}_0 - \delta$ may be used. For the plots in Fig. 9 the atomic line is at the left axis. A full cone spectrum would involve summing the terms in Eq. (34) and producing one contour plot. We have not done this because of the lack of significant predicted gain. However, the general shape of the cones displayed in Fig. 9 do show similar characteristics to those of the experimental cone in Fig. 8. Both plots of Fig. 9 shows on-axis red light near the atomic transition and the characteristic $\sqrt{N/\omega}$ shape. Also both plots show the transition toward a constant, nonzero angle at large detunings from ω_0. The two plots of Fig. 9 are repeated in Fig. 11 with $\sqrt{N/\omega}$ lines overlaid, along with other cone results.

Gain. Figure 10 shows relative gain of each sideband that, for example, is defined for the red sideband by

$$g_r = \frac{P_{\text{out}} - P_{\text{in}}}{P_{\text{seed}}}, \tag{43}$$

where P_{out} is the red sideband output power, P_{in} is the input power, and P_{seed} is the seed input power.

The upper limit of relative gain that would occur without diffraction can be obtained by considering a ring of thickness $\Delta\tilde{r}$ at a radius $\tilde{r}_g$, where the sidebands are expected to receive gain. By the exit plane the input seed will retain the same shape as a result of neglecting diffraction, but will now have a large intensity spike at $\tilde{r}_g$ with a thickness of $\Delta\tilde{r}$. If a Gaussian radial profile is used for the input seed the relative gain can be written as

$$g_r \sim \left\{ 2.77 \left(\frac{\tilde{r}_g \Delta\tilde{r}}{\tilde{r}_{1/2}^2} \right) \exp\left[-1.386 \left(\frac{\tilde{r}}{\tilde{r}_{1/2}} \right) \right]^2 \right\} e^{2\tilde{\mu}_+ z}. \tag{44}$$

Estimating the values of $\tilde{r}_g$ and $\Delta\tilde{r}$ to be 6 μm and 2 μm from Fig. 5, respectively, it is possible to calculate $g_r = 0.05 e^{2\overline{\mu}_+ z} \approx 2.56 \times 10^{33}$. This value is 34 orders of magnitude larger than what is calculated and presented in Fig. 10, demonstrating that diffraction plays a crucial role and plane-wave solutions are not appropriate. However, the gains presented are much less than what is observed in the experiment.

2. The search for gain

The lower limit of gain needed to see conical emission in the experiment is about 1×10^8, that is, the product $\overline{\mu}_+ \times z_{\text{cell}}$ must be greater than 10. This estimate comes from assuming one photon initiating the coherent process that produces the cone. It is apparent from the sudden turn-on of the unseeded field in Figs. 6 and 7 that it is possible to produce a large $\overline{\mu}_+$, but only for very short distances. The parameters relevant for the search for gain are as follows. (1) The scaled dimensionless power of the laser (Φ/Φ_K). (2) The dimensionless radius of the laser $(r_{1/2})$. (3) The radial shape of the laser. (4) The free-space focus of the laser and/or the sideband seed. (5) The detuning (δ) of the sideband from $\mathcal{R}_o$. (6) The radial shape of the input seed. (7) Phase fluctuations in the laser. (8) Amplitude fluctuations of the laser. (9) The Doppler width. (10) The time of sideband propagation, only relevant for sideband propagation during a time-dependent laser pulse. For the gain to be considered realistic, at least an increase of 5 orders of magnitude over what has been calculated previously is needed. Due to this large factor, in the following discussion only qualitative descriptions will be used.

A Powell method was used to attempt to find the maximum gain while varying the parameters Φ/Φ_K, $r_{1/2}$, and δ. Different starting values gave different ending values, as would be expected simply by looking at any one of the relative gain plots shown in the detuning scans. But none of the maximization runs gave gains that were orders of magnitude larger than what has been previously calculated.

The radial shape of the laser beam has been changed to be more flat topped. This widens the optimal interaction region that produces more gain, but not much. Other radial shape changes also did not change the gain of the sidebands by any significant amount. Stationary solutions for the laser beam have been used which maintain their radial shape during propagation, resulting in the optimal interaction region not moving around in $\tilde{r}$ and z which increases the gain length. No significant increase in gain was observed. Changing the radial shape of the input seed made even smaller changes in the gain of the sidebands. The shape of the laser and the shape of the input seed is a difficult parameter to adjust in a systematic way. However, it is also believed that the gain should not be significantly affected by shape, because cone emission is seen in the experiments with good Gaussian beams as well as poorly shaped beams.

In the sideband propagations shown earlier the blue sideband was seen to diffract. This motivated moving the free-space focus of the seed and the laser from the input face to the middle of the cell, hoping that the optimal interaction region would track the diffracting blue sideband in such a way that both sidebands would receive more gain. Again there was no significant increase in the gain for either sideband.

Rapid intensity fluctuations of the laser could possibly increase the gain. Testing this possibility requires a time-dependent calculation for the laser. Our procedure is first to calculate the time-dependent laser propagation up to some time T_c, at which time a sideband propagation is done. However, before a sideband propagation is done the laser field is multiplied by a constant, then repropagated through the medium at this time step. After this propagation the value of $\Omega_l(\tilde{r},z,T_c)$ has been adjusted in response to the intensity fluctuation, and the values of $\mathcal{D}(\tilde{r},z,T_c)$, and $\sigma(\tilde{r},z,T_c)$ in Eqs. (31a) through (31d) remain unchanged. At this point a sideband propagation is performed. This method was used at a variety of T_c values with and without fluctuations in the intensity. Again there was no significant change in the achieved gain.

Phase fluctuation can be added as a first approximation by assuming a Lorentzian distribution of width γ_l for the fluctuations in $\dot{\Phi}$. After performing a convolution of a Lorentzian with the $\overline{\alpha}$'s and $\overline{\chi}$'s the result is the addition of the phase fluctuation width (γ_l) to the a in Eqs. (31a) through (31d). This additional width makes the optimal interaction region wider, i.e., makes the path length longer but it also decreased the effective $\overline{\mu}_+$ value. The net result of longer path lengths and smaller effective $\overline{\mu}_+$ values is no significant change in the gain.

Changing the Doppler width has a similar effect on the gain. Again a wider optimal interaction region is created with increased Doppler width, but along with this increased width comes decreased effective $\overline{\mu}_+$ values. Therefore, as before with the inclusion of phase fluctuations, there is no change in the achieved gain. At this level, this might be used as an argument to not include Doppler averaging in the calculations. However, as the Doppler width goes to zero the width of the optimal interaction region becomes so narrow that the numerics become increasingly difficult.

It is encouraging to see that this model produces cone shapes very similar to those seen in the experiment, but at a smaller angle. However, there is a significant lack of predicted gain on both of the sidebands. This surprising result implies that additional physics, not accounted for in the cylindrically symmetric model, must be accounted for in order to predict realistically large gains.

IV. DISCUSSION

The current leading models attempting to account for cone emission angles are Cherenkov-type emission [9,30], four-wave mixing with phase matching [15], refraction of the red sideband at the filament boundary [27], and a first-order perturbation theory [46]. All of these models reduce to the same result shown in Eq. (40). All of the physics that is included in any one of the previous models is included in the model presented in Sec. II. Yet we have shown that this physics does not, in fact, account for large CE gain in the case of large detuning and radial symmetry.

The advantage of a full propagation model as studied here is the ability to not only predict the cone angle, but the entire shape of the cone as seen on a plot of angle (θ) versus frequency (δ). The detuning scans shown in Fig. 9 for the far field of the red sideband are shown again in Fig. 11 with propagations done at other laser initial conditions. Superimposed on each graph are three plots of Eq. (40) with $k = 1.0$, 1.5, 2.0, the constant of proportionality in Eq. (40). The experimental values for k lay between 1.0 and 1.77. One of the experimental features of the cone is the constant angle tail at large δ, as shown in Fig. 8, which most definitely does not follow the scaling of Eq. (40). In plots (a), (b), and (d) of Fig. 11 one can see evidence of a constant angle tail for $|\Delta_0 - \mathcal{R}_0 - \delta| > 150$ GHz.

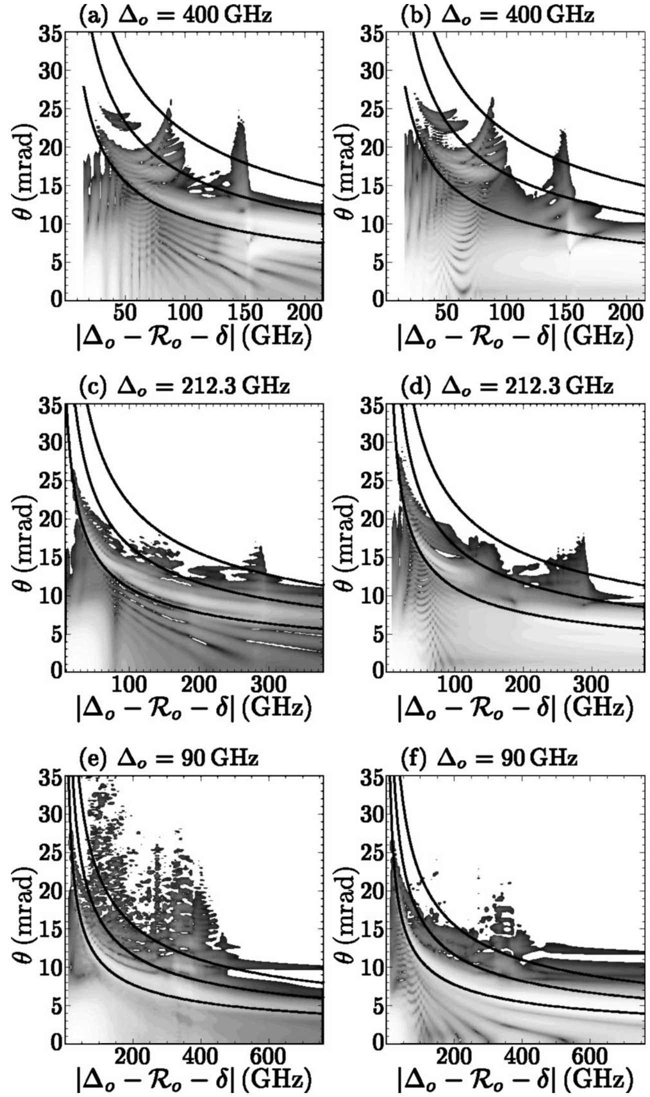

FIG. 11. A blue input seed was used for the propagation in the left column. A red input seed was used for the propagation in the right column. The solid lines are plots of Eq. (40) with $k = 1.0$, 1.5, 2.0. The value 0 GHz on the horizontal axis is the atomic transition.

As discussed in the Introduction, a full semiclassical steady-state calculation with diffraction has been done by Valley *et al.* [24,47] and it is qualitatively similar to that presented here. Their calculations were restricted to detunings, $\Delta \approx \nu_{\mathrm{FWHM}}$, where ν_{FWHM} is the Doppler width, and they did not assume cylindrically symmetry. (Their calculation used a fast Fourier transform (FFT) on a Cray supercomputer.) Doppler averaging was included for the laser propagation as well as for the propagation of the sideband because of the small laser detuning. The Valley calculation also includes a random seed β_i. Valley *et al.* [24] write as follows:

> The transverse dependence [through $\Omega_l(x,y,z)$] of the resonance fluorescence β_i from moving atoms is calculated for each frequency and each *x, y, z* using plasma-dispersion functions. Its phase is chosen arbitrarily between 0 and 2π by a random-number generator at each *x, y, z*.

They report very good qualitative agreement of their model calculation with experiment. They present gain on both sidebands with only the red sideband going into a cone. In the case of small detuning the radial variation of the $\overline{\alpha}$'s and the $\overline{\chi}$'s becomes much wider relative to the laser-beam width. Consequently one would qualitatively expect more gain. They do not comment on the propagation of the sidebands in the medium or the frequency-angle distribution of the cones.

Where is the gain?

During the extensive search of parameter space described in Sec. III B 2 and in all of the sideband propagations shown in Figs. 6 and 7, the blue sideband simply diffracts out of the optimal interaction region. *The lack of gain in the calculation appears to be a consequence of the lack of trapping of the blue sideband*. So the theoretical search for gain may be turned into a search for parameters that trap the blue sideband. The phenomenological α_c model presented in Sec. III A 1 shows that if the blue sideband is trapped there can be large gain for the red cone. Estimates of the critical angle for trapping the blue sideband using $\Delta[n(r)-1]$ are always smaller than the diffraction angle for the blue sideband. This is only a rough result because when the two sidebands are strongly coupled via the $\overline{\chi}$'s, the concept of an index of refraction is unclear.

Once cylindrical symmetry is assumed (no dependence on azimuthal angle ϕ), the fields are restricted to $m=0$ modes, where m is the azimuthal mode number. It is known that the free diffraction of a field of the form $\varepsilon(r)e^{im\phi}$ with $m\neq 0$ will have zero intensity at $r=0$ for every z. It is possible to envision a ray picture for a combination of these modes. The ray picture corresponds to a "skew mode" that never passes through the origin. This skew mode ray may be imagined as being trapped in a radial index of refraction, spiraling around the z axis.

Imagine a radial index of refraction with the form of $\overline{\alpha}_b(\tilde{r})$ [from Eq. (31b)], which contains the blue index of refraction and the blue three-photon gain. The shape of $\overline{\alpha}_b(\tilde{r})$ is proportional to $-\overline{\alpha}_r^*(\tilde{r})$, which is shown in Fig. 5. There are two regions in which $(d/dr)(\mathrm{Im}[\overline{\alpha}_b(\tilde{r})])<0$, which are candidates for trapping a skew mode. It is known that blue sidebands with $m=0$ are not trapped. These $m=0$ modes correspond to rays that pass through the origin. But, instead, imagine an off-axis ray that is given in an initial input direction such that it spirals around the z axis. The ray is then able to skim the radial index of refraction with a smaller grazing angle. There may come a point where this angle will be small enough to allow for total internal reflection, which leads to trapping of the blue sideband. A waveguide analogy to this would be the modes near the cut-off mode in a concentric cylinder geometry. The important difference is that instead of the cut-off mode being damped, the blue sideband would actually experience greater gain because of increased path length. In other words, the slower the mode propagates the bigger its gain. It is now possible to imagine this trapping region oscillating in $\overline{\tau}$ along z as was seen in plots (c) and (g) of Figs. 6 and 7.

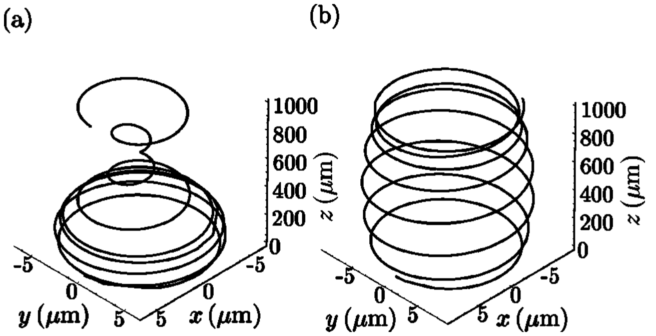

FIG. 12. Ray path of skew modes. Plots (a) and (b) show the path of a ray in three dimensions as it spirals around the *z* axis.

A generalization of Snell's law has been used to test this possibility. In every case that was tried it was possible to find a skew ray at the blue sideband frequency that would remain trapped. In this picture it is possible to increase the path length without bound and, therefore we presume, get an arbitrarily large amount of gain. Two examples of ray paths are shown in Fig. 12. Plot (a) corresponds to trapping a ray in the inner region, where plot (b) corresponds to trapping in the outer region.

The cylindrically symmetric code has been modified to accommodate an input field with $m\neq 0$. The first successful test of the code was to propagate a stationary laser mode with $m\neq 0$. The inclusion of $m\neq 0$ modes adds two more parameters to the search for gain. There is m_b for the blue sideband and m_r for the red sideband. In principle, there is an m_l for the laser, but in the experiment the input beam is a Gaussian that requires $m_l=0$. With no prior knowledge of the values of the m's, the search for gain can be rather tedious. Only a few combinations of m values have been tried. The ray picture involves a sum of very large m values, which are difficult to propagate even in the modified code. Preliminary simulations did not show large gain.

A steady-state FFT calculation has also been attempted. An FFT calculation done on an x-y grid, in principle, can propagate all m values at once. However, the numerical requirements exceeded our computational resources (DEC alpha 333 MHz). A time-dependent FFT calculation for the large detunings needed to match our experimental calculations requires much smaller time steps and finer x-y grid spacing than were needed by Valley *et al.*

The gain seen by Valley *et al.* in their FFT-based simulations is believed by us to have been achieved because of radially wider trapping index of refraction than the trapping index of refraction found for the large detunigns that we are interested in modeling. But, more importantly, the seeding of $m \neq 0$ modes via random phase of their β_i terms at each x, y, z point. Valley *et al.* make no mention of blue sideband trapping or propagation of specific $m \neq 0$ modes. As a result of using an FFT method for the propagation, there is no need to ask questions about different m modes. Only after propagating $m=0$ modes with very little gain does the importance of $m \neq 0$ modes become apparent.

At present, we believe that noncylindrically symmetric $(m \neq 0)$ trapped modes of the sidebands are a likely explanation for the observed experimental gain. If the blue sideband was trapped, the achievable gain lengths would be greatly increased. This expectation is strengthened by the calculations presented in Sec. III A 1, and by the observation in experiments that the blue-detuned emission at the 4WM frequency is much weaker than CE, and the blue-detuned light that does escape the cell is predominately on axis. This suggests a need for new simulations that use the state-of-the-art computer resources.

V. A NEW MODEL FOR CONE EMISSION

A complete model for the propagation that describes a time-dependent laser beam with large detuning relative to the natural line width and weak spectral sidebands has been presented. The density-matrix equations have been cast into the dressed-atom frame to eliminate the strong coupling and rapid temporal oscillations present in the bare-atom frame. The dressed-atom frame also allows the expansion of coefficients in the field equations to order $\gamma/\mathcal{R}$. The sidebands are assumed to be symmetrically detuned about the laser with large detuning relative to the width of the laser and the width of the sidebands. Also, the α_c model, an extension to the plane-wave FWM model developed by Boyd *et al.* [30], has been presented.

One of the observations of cone emission that is difficult to explain is the large gain experienced by the red sideband in the forward cone direction along with the lack of gain for the blue sideband. The α_c model presented in Sec. III A 1 shows that if the blue and red sidebands are trapped inside the laser filament with some of the red light coherently escaping the filament, it is possible to predict more energy in the red-detuned cone than in the blue sideband.

The time-dependent theory presented in Sec. II is solved in steady state with cylindrical symmetry in Sec. III. As a result of making these approximations, transient propagation effects are lost, but more importantly is the restriction to the $m=0$ radial modes. This is inconsequential for the laser propagation because the input laser in the experiment is nearly Gaussian $(m=0)$. However, the sidebands are seeded with stochastic light that can, in principle, seed all m modes.

Even with the restriction of propagating only $m=0$ modes, much has been learned about the propagation of the sidebands. In Sec. III B it was shown that red sidebands with $m=0$ modes are directed into weak cones via refraction and phase matching. These red cones have frequency and angular distributions similar to those of cones seen in our experiment. It is important to point out that there are several cases where the red sideband is trapped in a filament smaller in radius than the laser filament. The boundary of this filament is where the region of optimal interaction between the red and blue sideband occurs. Also at this filament boundary, red light is directed into a cone. In contrast, the blue sideband with $m=0$ is only very slightly affected by the gradient in the index of refraction at the blue sideband frequency, resulting in the blue sideband diffracting out of the laser filament region. The α_c model presented in Sec. III A 1 implies that if the red and blue sidebands can be trapped inside a filament with the red sideband coherently leaking into a red cone, it is possible to produce more energy in the red cone than in both the blue and red on-axis filament. A generalization of Snell's law is used in Sec. IV A to show that it is possible to trap blue sidebands with large mode numbers $m \gg 0$.

From all of the calculations presented in this paper, a comprehensive picture of cone emission can be hypothesized. The medium, as modified by the laser, is seeded with stochastic light. For the blue sideband it is known that modes with small m values will diffract out of the filament region, receiving very little gain. A blue sideband with large m values will be able to be trapped inside the laser filament where it will be able to interact with the laser and red sideband. This results in the blue sideband modes with large m values receiving more gain than modes with small m values. It is known that the $m=0$ mode for the red sideband can be trapped and therefore can receive gain. Also the red sideband with $m=0$ can produce a cone in the far field. However, the gain preference for different m modes for the red sideband is not known. Inside the laser filament a red sideband with a strong $m=0$ mode component and a blue sideband with strong $m \gg 0$ components will be trapped. The blue sideband will receive gain via three-photon gain from the laser. This blue light will then couple with the red sideband to produce red gain. This red light, which is partially trapped, will also coherently leak out of the filament region to produce a cone in the far field. The greater the rate at which the red light is coherently leaked into the cone, the weaker the blue filament will become. In effect, the blue receives energy from the laser via three-photon gain. This is then transferred to the red sideband, which in turn produces a red cone.

Given this model, conservation of photon orbital angular momentum $\hbar m$ (not to be confused with photon spin, or polarization [48]) would imply that the red cone would be generated with orbital angular momentum opposite to that of the blue light. In particular, when only linearly polarized light is present, there should be no red cone light generated with $m=0$. This prediction suggests that a new class of experiments, in which orbital angular momentum is measured, could be carried out in order to test this conjectured new model.

ACKNOWLEDGMENTS

M.G.R. wishes to thank JILA for hospitality extended during his stay. We thank Wojciech Gawlik and David Sarkisyan for their valuable suggestions. This work has been supported in part by the National Science Foundation.

[1] C. Sacchi, C. Townes, and J. Lifsitz, Phys. Rev. **174**, 439 (1968).
[2] M. Ter-Mikaelian, G. Torossian, and G. Grigoryan, Opt. Commun. **119**, 56 (1995).
[3] T. Shevy and M. Rosenbluh, J. Opt. Soc. Am. B **5**, 116 (1988).
[4] A. Plekhanov, S. Rautian, V. Safonov, and B. Chernobrod, Zh. Eksp. Teor. Fiz. **88**, 426 (1985) [Sov. Phys. JETP **61**, 249 (1985)].
[5] E. Chauchard and Y. Meyer, Opt. Commun. **52**, 141 (1984).
[6] Y. Meyer, Opt. Commun. **34**, 439 (1980).
[7] D. Harter, P. Narum, M. Raymer, and R. Boyd, Phys. Rev. Lett. **46**, 1192 (1981).
[8] I. Golub, G. Erez, and R. Shuker, Opt. Commun. **57**, 143 (1986).
[9] I. Golub, G. Erez, and R. Shuker, J. Phys. B **19**, L115 (1986).
[10] A. Dreischuh, V. Kamenov, S. Dinev, U. Reiter-Domiaty, D. Gruber, and L. Windholz, J. Opt. Soc. Am. B **15**, 34 (1998).
[11] V. I. Vaichaitis, M. V. Ignatavichyus, V. A. Kudryashov, and Y. N. Pimenov, Pis'ma Zh. Eksp. Teor. Fiz. **45**, 327 (1987) [JETP Lett. **45**, 414 (1987)].
[12] D. Chekhov, D. Gaidarenko, A. Leonov, A. Panteleev, and A. Starostin, Opt. Commun. **105**, 209 (1994).
[13] D. Grischkowsky, Phys. Rev. Lett. **24**, 866 (1970).
[14] W. Chalupczak, W. Gawlik, and J. Zachorowski, Phys. Rev. A **49**, 4895 (1994).
[15] C. Skinner and P. Kleiber, Phys. Rev. A **21**, 151 (1980).
[16] W. Chalupczak, W. Gawlik, and J. Zachorowski, Opt. Commun. **99**, 49 (1993).
[17] M. Fernandez-Guasti, J. Hernandez-Pozos, E. Haro-Poniatowski, and L. Julio-Sanchez, Opt. Commun. **108**, 367 (1994).
[18] G. Brechignac, P. Cahuzac, and A. Debarre, Opt. Commun. **35**, 87 (1980).
[19] R. Hart, L. You, A. Gallagher, and J. Cooper, Opt. Commun. **111**, 331 (1994).
[20] W. Chałupczak, W. Gawlik, B. Lobodzińsik, T. Pałasz, G. Wąsik, J. Zachorowski, and B. Samson, in International Symposium on Atomic Coherence and Inversionless Optical Amplification (unpublished).
[21] M. Dowell, R. Hart, A. Gallagher, and J. Cooper, Phys. Rev. A **53**, 1775 (1996).
[22] B. Paul, M. Dowell, A. Gallagher, and J. Cooper, Phys. Rev. A **59**, 4784 (1999).
[23] D. Sarkisyan, B. Paul, S. Cundiff, E. A. Gibson, and A. Gallagher, J. Opt. Soc. Am. B **18**, (2001).
[24] J. Valley, G. Khitrova, H. Gibbs, J. Grantham, and X. Jiajin, Phys. Rev. Lett. **64**, 2362 (1990).
[25] Y. Ben-Aryeh, Phys. Rev. A **56**, 854 (1997).
[26] L. You, J. Mostowski, J. Cooper, and R. Shuker, Phys. Rev. A **44**, R6998 (1991).
[27] D. Harter and R. Boyd, Phys. Rev. A **29**, 739 (1984).
[28] M. Crenshaw and C. Cantrell, Phys. Rev. A **39**, 126 (1989).
[29] J. Guo, J. Cooper, and A. Gallagher, Phys. Rev. A **52**, R3440 (1995).
[30] R. Boyd, M. Raymer, P. Narum, and D. Harter, Phys. Rev. A **24**, 411 (1981).
[31] P. Meystre and M. S. Sargent III, *Elements of Quantum Optics*, 2nd ed. (Springer-Verlag, Berlin, 1991).
[32] M. Dowell, B. Paul, A. Gallagher, and J. Cooper, Phys. Rev. A **52**, 3244 (1995).
[33] L. You, Ph.D. thesis, University of Colorado, 1993.
[34] L. You, J. Cooper, and M. Trippenbach, J. Opt. Soc. Am. B **8**, 1139 (1991).
[35] B. D. Paul, Ph.D. thesis, University of Colorado, 1999.
[36] J. Eberly and K. Wodkiewicz, J. Opt. Soc. Am. **67**, 1252 (1977).
[37] B. Mollow, Phys. Rev. **188**, 1969 (1969).
[38] Y. Chen, Opt. Commun. **82**, 255 (1991).
[39] R. Y. Chiao, E. Garmire, and C. H. Townes, Phys. Rev. Lett. **13**, 479 (1964).
[40] E. Dawes and J. Marburger, Phys. Rev. **179**, 862 (1969).
[41] Z. Jovanoski and R. Sammut, J. Nonlinear Opt. Phys. Mater. **6**, 209 (1997).
[42] M. Karlsson, Phys. Rev. A **46**, 2726 (1992).
[43] M. Le Berre, E. Ressayre, A. Tallet, and F. Matter, J. Opt. Soc. Am. B **2**, 956 (1985).
[44] W. H. Press, S. A. Teukolsky, W. T. Vetterling, and B. P. Flannery, *Numerical Recipes in* FORTRAN (Cambridge University Press, Cambridge, 1992).
[45] P. Drummond, Comput. Phys. Commun. **29**, 211 (1983).
[46] M. LeBerre-Rousseau, E. Ressayre, and A. Tallet, Opt. Commun. **36**, 31 (1981).
[47] J. F. Valley, Ph.D. thesis, University of Arizona, 1989.
[48] L. Allen, J. Courtial, and M. J. Padgett, Phys. Rev. E **60**, 7497 (1999).